Check for updates

Rotavirus Spike Protein VP4 Mediates Viroplasm Assembly by Association to Actin Filaments

Janine Vetter,[a] Guido Papa,[b*] Michael Seyffert,[a] Kapila Gunasekera,[c] ⓘGiuditta De Lorenzo,[b]§ Mahesa Wiesendanger,[a,d] Jean-Louis Reymond,[c] ⓘCornel Fraefel,[a] Oscar R. Burrone,[b] ⓘCatherine Eichwald[a]

[a]Institute of Virology, University of Zurich, Zurich, Switzerland
[b]Molecular Immunology Laboratory, International Centre for Genetic Engineering and Biotechnology, Trieste, Italy
[c]Department of Chemistry and Biochemistry and Pharmaceutical Sciences, University of Bern, Bern, Switzerland
[d]Institute of Anatomy, Vetsuisse, University of Zurich, Zurich, Switzerland

Janine Vetter and Guido Papa contributed equally to this work. Author order was determined by discussion and agreement among all the authors.

ABSTRACT Rotavirus (RV) viroplasms are cytosolic inclusions where both virus genome replication and primary steps of virus progeny assembly take place. A stabilized microtubule cytoskeleton and lipid droplets are required for the viroplasm formation, which involves several virus proteins. The viral spike protein VP4 has not previously been shown to have a direct role in viroplasm formation. However, it is involved with virus-cell attachment, endocytic internalization, and virion morphogenesis. Moreover, VP4 interacts with actin cytoskeleton components, mainly in processes involving virus entrance and egress, and thereby may have an indirect role in viroplasm formation. In this study, we used reverse genetics to construct a recombinant RV, rRV/VP4-BAP, that contains a biotin acceptor peptide (BAP) in the K145-G150 loop of the VP4 lectin domain, permitting live monitoring. The recombinant virus was replication competent but showed a reduced fitness. We demonstrate that rRV/VP4-BAP infection, as opposed to rRV/wt infection, did not lead to a reorganized actin cytoskeleton as viroplasms formed were insensitive to drugs that depolymerize actin and inhibit myosin. Moreover, wild-type (wt) VP4, but not VP4-BAP, appeared to associate with actin filaments. Similarly, VP4 in coexpression with NSP5 and NSP2 induced a significant increase in the number of viroplasm-like structures. Interestingly, a small peptide mimicking loop K145-G150 rescued the phenotype of rRV/VP4-BAP by increasing its ability to form viroplasms and hence improve virus progeny formation. Collectively, these results provide a direct link between VP4 and the actin cytoskeleton to catalyze viroplasm assembly.

IMPORTANCE The spike protein VP4 participates in diverse steps of the rotavirus (RV) life cycle, including virus-cell attachment, internalization, modulation of endocytosis, virion morphogenesis, and virus egress. Using reverse genetics, we constructed for the first time a recombinant RV, rRV/VP4-BAP, harboring a heterologous peptide in the lectin domain (loop K145-G150) of VP4. The rRV/VP4-BAP was replication competent but with reduced fitness due to a defect in the ability to reorganize the actin cytoskeleton, which affected the efficiency of viroplasm assembly. This defect was rescued by adding a permeable small-peptide mimicking the wild-type VP4 loop K145-G150. In addition to revealing a new role of VP4, our findings suggest that rRV harboring an engineered VP4 could be used as a new dual vaccination platform providing immunity against RV and additional heterologous antigens.

KEYWORDS rotavirus, spike protein, viroplasm, VP4, reverse-genetics, actin, reverse genetic analysis, spike

Address correspondence to Catherine Eichwald, ceichwald@vetvir.uzh.ch.

*Present address: Guido Papa, MRC Laboratory of Molecular Biology, Cambridge, United Kingdom.

§Present address: Giuditta De Lorenzo, MRC-University of Glasgow, Centre for Virus Research, Glasgow, United Kingdom.

Rotavirus (RV) is the primary etiological agent responsible for severe gastroenteritis and dehydration in infants and young children worldwide (1), resulting in the death of 128,000 children under 5 years of age in developing countries. Moreover, it also infects young animals such as piglets, calves, and poultry, negatively impacting the livestock industry (2–4).

RV virions are nonenveloped icosahedral particles composed of three concentric layers, called triple-layered particles (TLPs). The virus core shell encloses 11 double-stranded (ds) RNA genome segments and 12 copies of the RNA-dependent RNA polymerase, VP1, and the guanyl-methyltransferase, VP3 (5, 6). The icosahedral core shell (T = 1, symmetry) is composed of 12 decamers of VP2 and surrounded by 260 trimers of the structural protein VP6, constituting transcriptionally active double-layered particles (DLPs) (7, 8). Trimers of VP7 glycoprotein are organized in an icosahedral symmetry (T = 13) stand on the top of each VP6 trimer constituting the main building component of the virion outer layer. The spike protein VP4 anchors at each of the virion 5-fold axes adopting a trimeric conformation, although they have a dimeric appearance when visualized from the top of the capsid surface (9–12).

Immediately after RV internalization, the DLPs are released into the cytoplasm and become transcriptionally active (13), leading to the first round of transcription, which is necessary for halting the host innate immune response (14–18), shutting off the host translation machinery (19), and starting the building-up of viroplasms (20–22). The RV cytosolic replication compartments, termed viroplasms, are membraneless electron-dense globular inclusions responsible for virus genome replication and virus progeny assembly (20, 23). The RV proteins NSP5, NSP2, and VP2 are the assembling blocks for viroplasms (24). Other virus proteins are also found in the viroplasms, including NSP4, VP1, VP3, and VP6, together with double-stranded and single-stranded viral RNAs. Host components, such as microtubules, lipid droplets, or miRNA-7 (25–27), are also recruited to viroplasms. The formation of viroplasms requires reorganizing and stabilizing the microtubule network and the recruitment of lipid droplets in a process directly associated with NSP2 and VP2. Thus, the viroplasms coalesce from small-punctuated structures diffused in the cytosol at early times postinfection to large perinuclear mature inclusions at late times of infection (25, 26, 28). However, there is evidence suggesting that in addition to microtubules, actin and intermediate filaments also reorganize under RV infection by using a mechanism (25, 29). Many virus proteins have multifunctional roles during the viral life cycle, and the RV proteins are no exception. An example is VP4, which is cleaved by a trypsin-like enzyme found in the intestinal tract (30) into two main products, VP8* (28 kDa, amino acids 1–247) and VP5* (60 kDa, amino acids 248–776), that remain noncovalently associated with the infectious particle allowing the initiation of the RV entry process (31, 32). VP8* and a significant portion of VP5*, VP5CT (amino acids 246–477), constitute the distal globular and the central body of the spike, respectively (33, 34). The VP8* subunit has hemagglutinin activity (35), is involved in host sialic acid binding (34), and has a determinant role in virus tropism. VP5* has been implicated in the interaction with integrins (36–38). During virus internalization, VP4 engages the endocytic pathway (39, 40) by binding to the small GTPase Rab5 and PRA1 within early endosomes (41), directly activating hsp70 (42, 43) and associating with the actin-binding protein Drebrin 1, an RV restriction factor (44). Additionally, VP4 plays an essential role in virion morphogenesis and can be found as a soluble protein in the cytosol (45). When expressed in the absence of other RV proteins, VP4 is associated with the microtubules and the actin cytoskeleton (45–50). In polarized cells, VP4 seems to interact with the apical actin cortex, leading to the remodeling of the brush border and subsequently releasing the RV virions into the medium (48). This actin association is dependent on a VP4 actin-binding domain present at its C-terminus (residues 713–776) in cooperation with the coiled-coil domain (residues 481–574) (45). However, there is no direct evidence that VP4 participates in actin reorganization during RV infection.

Here, we describe the generation of a recombinant RV (rRV) harboring a genetically modified genome segment 4 (gs4) encoding the spike protein VP4 with a biotin-acceptor peptide (BAP) tag of 15 amino acids inserted in an exposed loop of VP8*

(residues K145–G150). Even though rRV/VP4-BAP is internalized and able to produce virus progeny, it has significantly reduced virus fitness that correlates with an impaired ability of VP4-BAP to associate with actin filaments. In addition, we provide clear evidence that VP4 facilitates viroplasm assembly in an actin-dependent process.

RESULTS

Production and analysis of recombinant rotavirus harboring a BAP tagged spike protein. As the VP4 spike protein plays an essential role in the host cell tropism, attachment, and internalization, we addressed if VP4 could be engineered by incorporating a heterologous peptidic tag within its coding sequence without compromising its structural and functional properties. To test this hypothesis, we identified in the previously published crystal structure of simian RRV VP4 (10) four different exposed loops localized in the lectin domain (amino acids 65–224) of the VP8* subunit and then inserted a biotin acceptor peptide (BAP) tag (51, 52) in each of the corresponding loops of the VP4 simian strain SA11. As depicted in Fig. 1a, the selected loops for the BAP tag insertions were T96-R101, E109-S114, N132-Q137, and K145-G150, labeled with the colors blue, orange, pink, and green, respectively. First, we assessed the biotinylation of these four BAP-tagged VP4 proteins, herein VP4-BAP, in cell lysates by Western blot-retardation assay (WB-ra) (51). For this purpose, each construct was coexpressed with cytosolically localized biotin ligase Bir A (cyt-BirA) in MA104 cells infected with recombinant vaccinia virus encoding T_7 RNA polymerase to allow the synthesis of cytosolic VP4 transcripts. As the synthesis of nuclear VP4 transcripts promotes undesired mRNA splicing (53), we used a T_7 promoter to favor cytosolic transcription provided by the T_7 RNA polymerase. As shown in Fig. 1b, the four VP4-BAP variants (Fig. 1b, lanes 4, 6, 8 and 10), but not the wild-type (wt) VP4 (Fig. 1b, lane 2), were fully biotinylated. When the cell extracts were incubated with streptavidin (StAv), a shifted band of approximately 140 kDa was generated corresponding to the VP4–BAP/StAv complex. Of note, biotinylated protein-StAV complexes hinder epitopes of the biotinylated protein denoted as a shifted and weaker band in Western blot. The band observed immediately above the VP4-BAP band (80 kDa) represents a phosphorylated form of the protein that is only present in transfected cells but not in RV-infected cells, as demonstrated by the λ-phosphatase treatment of the cellular extracts (Fig. S1a and b posted at https://zenodo.org/record/6865927#.YtfEH-xBw-Q). This result suggests that the expression and stability of the four different VP4-BAP proteins were not affected by the location of the inserted BAP tag.

Next, we assessed whether the four VP4-BAP proteins could assemble into infectious RV particles and support virus replication. To rescue recombinant rotavirus (rRV) harboring a genetically modified genome segment 4 (gs4) encoding for the different VP4-BAP proteins (gs4-BAP), we took advantage of the previously established reverse genetics system (54). Of the four different constructs, we successfully rescued only the rRV harboring gs4-BAP encoding the BAP tag within the K145–G150 loop in VP8* (Fig. 1a), herein named rRV/VP4-BAP. The rescued virus was confirmed by the differential migration pattern of the modified gs4-BAP compared to the wt gs4 (Fig. 1c) and by Sanger sequencing (Fig. 1d). Notably, the genome segment 4 (gs4-BAP) and all of the other 10 genome segments of rRV/VP4-BAP were stable in tissue culture at least until virus passage 10 as determined by Sanger sequencing and deep sequencing (Fig. S1b and supplemental material posted at https://zenodo.org/record/6865927#.YtfEH-xBw-Q). We then investigated the ability of rRV/VP4-BAP to express biotinylated VP4-BAP. Specifically, cell extracts of rRV/VP4-BAP-infected MA/cytBirA cells (MA104 cells stably expressing cytosolic localized BirA) were analyzed at 6 hours postinfection (hpi) by Western blot. Thus, the produced VP4-BAP protein showed to be biotinylated as demonstrated by incubation with StAv-peroxidase, which detected a band of approximately 85 kDa only in extracts from rRV/VP4-BAP-infected MA/cytBirA cells, but not from rRV/VP4-BAP-infected MA104 cells (Fig. 1e, lanes 3 and 6). As expected, VP4 biotinylation was detected neither in rRV/wt-infected MA/cytBirA cells nor in rRV/VP4-BAP-
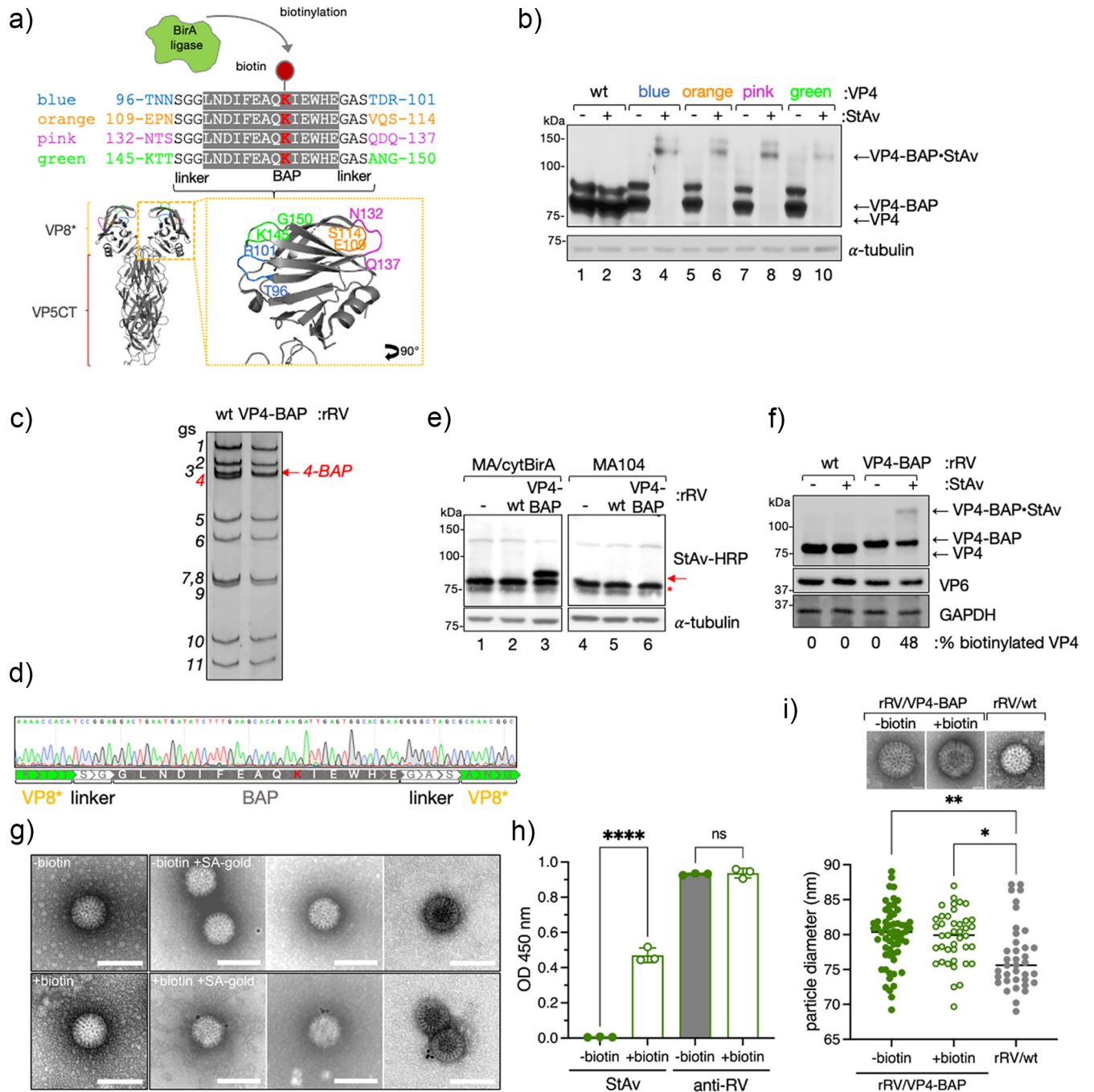
FIG 1 Generation of VP4-BAP tagged recombinant rotavirus. (a) Schematic representation of BAP tag inserted into the lectin domain loops of the VP8* subunit of VP4 from RV simian strain SA11 (GenBank: X14204.1). The lysine (K, red) indicates the biotinylation site of BirA ligase. Four different VP4 proteins tagged with BAP (VP4-BAP) were built between amino acid regions T96-R101 (blue), E109-S114 (orange), N132-Q137 (pink), and K145-G150 (green). VP4 trimer ribbon structure is presented for the visualization of VP8* (yellow) and VP5CT (body and stalk, red) fragments. An inset in VP8* indicates the different positions in the hydrophobic loops of VP8* where the BAP tags were inserted and colored in blue, orange, pink, and green. (b) Immunoblot retardation assay of cell lysates transiently expressing wtVP4 and VP4-BAP, tagged at blue, orange, pink, and green positions, respectively. Untreated (-) and streptavidin-treated (+) samples are indicated. The membrane was incubated with anti-VP4 to detect unbound VP4-BAP and VP4-BAP bound to streptavidin (VP4-BAP•StAv). α-tubulin was used as a loading control. (c) dsRNA electropherotype of the genome segments of rRV/wt and rRV/VP4-BAP. The red arrow points to gs4-BAP. (d) Sequence chromatogram of gs4 of rRV/VP4-BAP. The sequence indicates the position of the linkers and the BAP tag in between the VP8*. (e) Immunoblotting of uninfected (lanes 1 and 4) or infected cell lysates in MA-cytBirA cells (left panel) or MA104 cells (right panel) infected with either rRV/wt (lanes 2 and 5) or rRV/VP4-BAP (lanes 3 and 6) (MOI, 25 VFU/cell). Biotinylated proteins were detected with StAv-HRP. α-tubulin was used as a loading control. The red arrow and red star indicate biotinylated VP4-BAP and host undetermined biotinylated protein, respectively. (f) Immunoblot retardation assay of MA-cytBirA cell lysates infected with rRV/wt or rRV/VP4-BAP untreated or treated with StAv. The membrane was incubated with anti-VP4 and anti-VP6 for detection of the virus. GAPDH was used as a loading control. The percentage of biotinylated VP4 and VP4-BAP was normalized to VP6 expression. (g) Visualization at a high resolution of purified virions isolated from rRV/VP4-BAP-infected MA-cytBirA cells untreated

infected MA104 cells (Fig. 1e, lanes 2, 5, and 6). We found by WB-ra that the fraction of biotinylated VP4-BAP corresponds to 48% of the total protein (Fig. 1f).

We next examined if the biotinylated virus-encoded VP4-BAP was incorporated into newly assembled virus particles. For this, we purified rRV/VP4-BAP virions produced in MA/cytBirA cells in the absence or presence of biotin and visualized the virus particles by negative staining electron microscopy after incubation with StAv conjugated to gold particles. Thus, 53% of the virions produced in the presence of biotin were decorated with StAV-gold particles (Fig. 1g) but none in the unbiotinylated control particles. Similarly, indirect ELISA with identical amounts of unbiotinylated and biotinylated purified rRV/VP4-BAP revealed a signal upon StAV-peroxidase staining only for biotinylated samples. Furthermore, similar signals were observed in ELISA using an antirotavirus antibody (Fig. 1h). These outcomes collectively suggest that virus-encoded VP4-BAP is biotinylated and incorporated in newly formed RV particles. Interestingly, as shown in Fig. 1i, the rRV/VP4 particles appear to have a slightly larger diameter ($\sim$80 nm) when compared to rRV/wt particles ($\sim$75 nm) but were still in the range of TLPs (55).

Subcellular localization of rRV/VP4-BAP. We investigated the subcellular localization of the newly produced biotinylated VP4-BAP in rRV/VP4-BAP-infected cells at 6 hpi, a time point showing well-assembled viroplasms (25). For this, both rRV/wt and rRV/VP4-BAP-infected MA/cytBirA cells were incubated in the absence or presence of biotin for 4 h before fixation. Biotinylated VP4-BAP detected with StAv-Alexa 555 was found surrounding the viroplasms (stained anti-NSP5) (Fig. 2a). However, no StAv-Alexa 555 signal was detected in cells infected with either rRV/wt or rRV/VP4-BAP without biotin. Notably, the biotinylated VP4-BAP partially colocalized with trimeric VP7 in the endoplasmic reticulum (ER) (Fig. 2b). Additionally, the cytosolic distribution of VP4-BAP was similar to that of VP4 in rRV/wt-infect cells (Fig. 2c). These results suggest that the modification exerted in VP4-BAP does not impact VP4 subcellular localization in infected cells.

Impaired virus fitness of rRV/VP4-BAP. To compare the replication fitness of rRV/VP4-BAP with rRV/wt, we infected MA104 cells at equal multiplicity of infection (MOI) and harvested the virus at various time points until 48 hpi. As depicted in Fig. 3a, rRV/VP4-BAP showed a significantly delayed fitness curve compared to rRV/wt up to 48 hpi. Consistent with this result, a significantly reduced number of viroplasms per cell prevailed at 6 hpi in rRV/VP4-BAP-infected cells compared to rRV/wt (Fig. 3b). We found that rRV/VP4-BAP had up to one log less virus progeny than rRV/wt at 24 and 48 hpi. To investigate the delay in the virus replication, we infected cells with identical MOI (Fig. 3c) or an equal number of virus particles (Fig. 3d) and quantified cells showing viroplasms at 6 hpi. In both experimental conditions, we observed a significantly reduced ratio of cells containing viroplasms upon infection with rRV/VP4-BAP compared to rRV/wt.

Comparable entry processes between rRV/wt and rRV/VP4-BAP. Since VP4 has an essential role in virus-cell attachment, we interrogated whether the ability of rRV/VP4-BAP particles to bind to cells was impaired. To test this hypothesis, we performed a nonradioactive binding assay previously described by Zárate et al. (56) to compare the attachment to MA104 cells with different amounts of either rRV/wt or rRV/VP4-BAP. As depicted in Fig. 4a, no differences in cell attachment were observed among the two viruses. Of note, the antibody conditions used for the virus detection are in the linear range (Fig. S2a posted at https://zenodo.org/record/6865927#.YtfEH-xBw-Q). Moreover, biotin labeling did not hinder the virus-cell attachment; the same results for

FIG 1 Legend (Continued)

(–biotin, upper panel) or treated (+biotin, lower panel) with 100 μM biotin. After purification, the virions were labeled with streptavidin conjugated to colloidal gold (12 nm), followed by negative staining electron microscopy (right panel). The scale bar is 100 nm. (h) Detection of purified unbiotinylated (gray bars) and biotinylated (open bars) rRV/VP4-BAP particles. The particles were coated in an ELISA plate followed by binding to streptavidin-HRP or guinea pig antirotavirus followed by anti-guinea pig conjugated to HRP. The median from three independent experiments is shown (ordinary one-way ANOVA; ****, $P < 0.0001$). (i) Scatter dot plot comparing the diameter of purified particles from unbiotinylated (–biotin, filled green dots) or biotinylated (+biotin, open green dots) RV/VP4-BAP and rRV/wt (filled gray dots). The median value is indicated, $n > 40$ particles, ordinary one-way ANOVA; *, $P < 0.05$; **, $P < 0.01$. Representative high-resolution images of negatively stained TLPs are visualized on top. Scale bar is 25 nm.
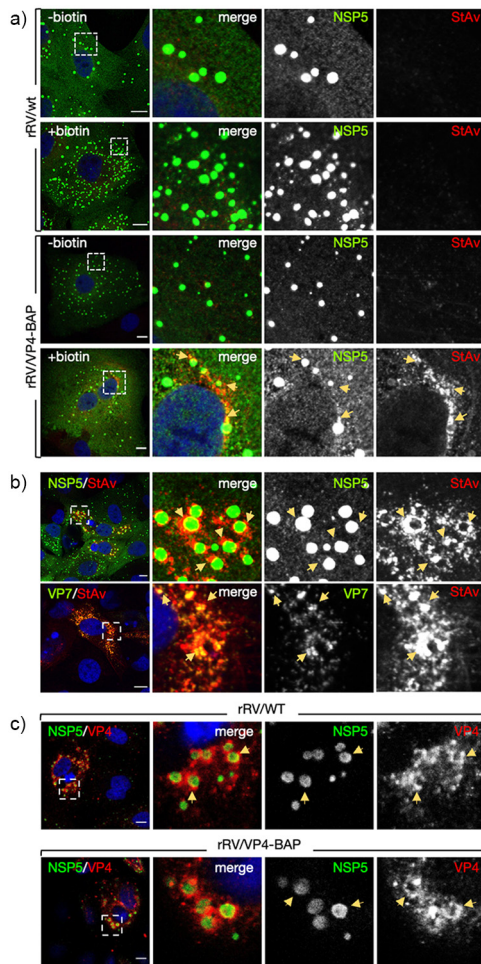
FIG 2 RV protein localization upon rRV/VP4-BAP infection. (a) rRV/wt (top panel) and rRV/VP4-BAP (bottom panel) infected MA-cytBirA cells were untreated (−biotin) or treated with biotin (+biotin). Cells were fixed with paraformaldehyde at 6 hpi and stained for the detection of viroplasms (anti-NSP5, green) and biotinylated proteins (streptavidin-Alexa 555, red). Nuclei were stained with DAPI (blue). (b) Immunostaining images of rRV/VP4-BAP-infected MA-cytBirA cells in the presence of biotin. At 6 hpi, paraformaldehyde-fixed cells were stained for the detection of VP4-BAP (StAv, red) in viroplasms (anti-NSP5, green) (upper row) or mature RV particles (anti-VP7 clone 159, green) (bottom row). (c) Immunofluorescence images of cells infected with rRV/wt (upper row) or rRV/VP4-BAP (lower row) comparing the localization of VP4 and VP4-BAP (anti-VP4, red), respectively. The viroplasms were detected with anti-NSP5 (green). Nuclei were stained with DAPI. In all of the figures, the dashed white boxes correspond to the image insets of the right columns. The yellow arrows point to the VP4-BAP or VP4 signal. The scale bar is 10 μm.

the attachment were obtained with both the unbiotinylated and the biotinylated rRV/VP4-BAP virus particles (Fig. 4b). As expected, binding of rRV/VP4-BAP was detected with StAV only when grown in the presence of biotin (Fig. 4c).

Next, we investigated whether the delay in viral replication fitness was caused by a difference in virus internalization. Purified rRV/VP4-BAP and rRV/wt virions were compared and analyzed for virus internalization by confocal scanning laser microscopy (CSLM) using immunostaining with the conformational monoclonal antibody anti-VP7 (clone 159), which only recognizes the trimeric form of the VP7 protein (57, 58). As a control, purified rRV/VP4-BAP, but not rRV/wt, was directly labeled with StrAv-Alexa 555 prior to infection. Initially (0 min), VP4-BAP and VP7 signals colocalized on the cell surface, indicating the association of virions to the cell membrane. However, after 2 min at 37°C, both signals were already internalized (Fig. 4d). The localization patterns were comparable to those observed at the same time points with rRV/wt virions, suggesting no differences in the internalization mechanism between the two viruses.
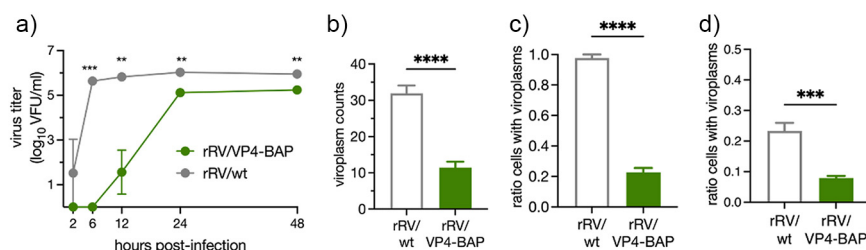
FIG 3 Replication fitness of rRV/VP4-BAP is delayed. (a) Virus replication fitness curve from 0 to 48 hpi of rRV/wt and rRV/VP4-BAP. The curve represents the mean of three independent experiments. Welch's t test; **, $P < 0.01$; ***, $P < 0.001$. (b) Plot for the quantification of viroplasm per cells at 6 hpi. Data correspond to the mean $\pm$ SEM, $n > 60$ cells. Welch's t test; ****, $P < 0.0001$. Quantification of cells with viroplasms of MA104 cells infected with rRV/wt and rRV/VP4-BAP at (c) same MOI (25 VFU/cell) or (d) the same numbers of virus particles. Samples were counted at 6 hpi ($n > 120$ cells). Welch's t test; ***, $P < 0.001$; ****, $P < 0.0001$.

Since virus-cell attachment and virus internalization were comparable between rRV/wt and rRV/VP4-BAP, we investigated if virus transcription was defective or delayed for rRV/VP4-BAP. Thus, we compared the abundance of NSP5 and VP6 virus transcripts at 4 hpi of MA104 cells infected with either rRV/wt or rRV/VP4-BAP. As denoted in Fig. 4e to g, the transcription levels of NSP5, VP6, and the housekeeping gene SDHA were comparable in cells infected with rRV/wt or rRV/VP4-BAP.

rRV/VP4-BAP has a defect in a step between virus transcription and viroplasm formation. We analyzed by high-definition electron microscopy the structural morphology of the viroplasms from rRV/wt and rRV/VP4-BAP at two time points, 6 and 12 hpi, which for simian strain SA11 correspond to a time showing well-formed viroplasms and a time with highly mature viroplasms, respectively (Fig. 5a). No apparent differences in the viroplasm morphology were observed between the two viruses at 6 and 12 hpi. Similarly, we examined whether the liquid–liquid phase separation properties of rRV/VP4-BAP viroplasms were modified. For this, we took advantage of our previously established MA104 cell line stably expressing NSP2-mCherry (MA/NSP2-mCherry) to visualize viroplasm formation in living cells because of the ability of this protein to get recruited into viroplasms during RV infection (21, 25, 59). The NSP2-mCherry diffusion dynamic in single viroplasms was then measured, using fluorescence recovery after photobleaching (FRAP) experiments (Fig. 5b and c). We found that FRAP properties concerning NSP2-mCherry half-time recovery and mobility were similar for both viruses (Fig. 5d and e).

To confirm our results and exclude the involvement of the endocytic pathway, we transfected MA104 cells with an equal number of purified DLPs obtained from the two viruses (Fig. 6a). Of note, purified rRV/wt DLPs or rRV/VP4-BAP DLPs had the same size, while rRV/VP4-BAP TLPs were larger than rRV/wt TLPs (Fig. 1i and 6a). At 6 h after transfection, we observed comparable expression of NSP5 for both viruses, as denoted by in-cell Western assay (Fig. 6b and c). In the same experimental setting, the number of cells showing viroplasms (detected with anti-NSP5) was significantly reduced in rRV/VP4-BAP-infected cells compared to rRV/wt-infected cells (Fig. 6d and e). These outcomes strongly suggest that the reduced replication fitness of rRV/VP4-BAP is due to partial impairment of viroplasm assembly.

VP4 promotes viroplasm assembly. As VP4 appears to have an unidentified role in the viroplasm assembly, we investigated if spontaneous disruption of the viroplasm led to a delayed reassembly of these structures. We used 1,6-hexanediol (1,6-HD), a well-described aliphatic alcohol able to disrupt key drivers of liquid–liquid phase separation and recently shown to be effective in dissolving RV viroplasms (28), to determine reassembly of viroplasm in infected MA/NSP2-mCherry cells. For this, MA/NSP2-mCherry cells were infected with either rRV/VP4-BAP or rRV/wt and at 5 hpi treated for 6 min with 1,6-HD and monitored for 30 min after washout of the compound (Fig. 7a and b). Interestingly, the recovery kinetic of rRV/VP4-BAP viroplasms was delayed
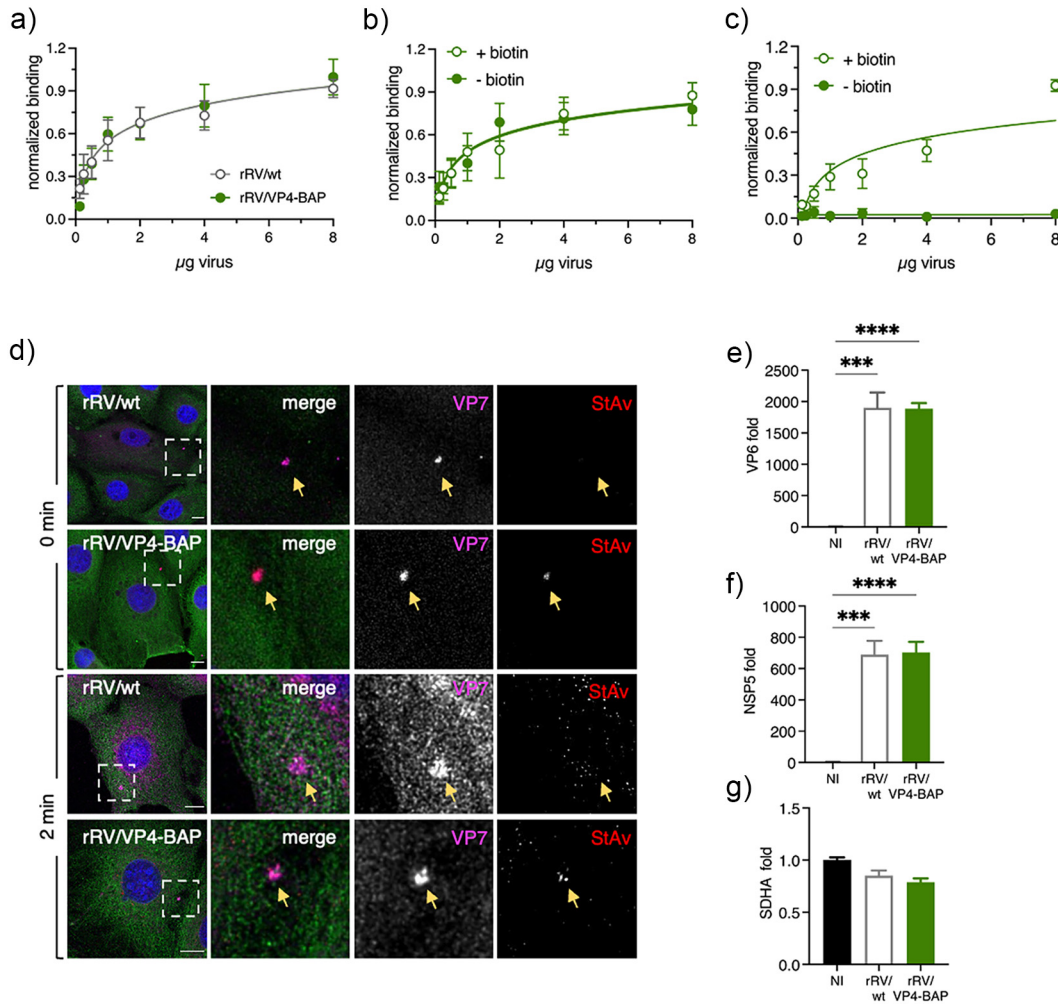
FIG 4 Virus attachment and internalization of RV/wt and rRV/VP4-BAP are comparable. (a) Virus attachment to MA104 cell surface with different amounts of purified rRV/wt (open gray dots) and rRV/VP4-BAP (full green dots). Samples were detected using a guinea pig anti-RV. The result corresponds to the mean of nine normalized independent experiments. Data analysis corresponds to nonlinear regression, $P = 0.2987$, $n = 9$. Virus attachment assay to MA104 cell surface with different amounts of unbiotinylated (−biotin, full green dots) and biotinylated (+biotin, green open dots) purified rRV/VP4-BAP detected with (b) guinea pig anti-RV followed by secondary antibody conjugated to HRP. Data analysis corresponds to nonlinear regression, $P = 0.6151$, $n = 6$. (c) Same as above, but samples were detected with streptavidin-HRP. Data analysis corresponds to nonlinear regression, $P < 0.0001$, $n = 6$. (d) Internalization of purified virions into MA104 cells at 0 min (upper panel) and 2 min (lower panel). Purified virions of rRV/wt and biotinylated rRV/VP4-BAP were previously labeled with StAv-Alexa 555 (red). At the indicated time postinfection, cells were fixed and immunostained for VP7 trimers (MAb anti-VP7 clone 159, pink) and MTs (anti-α-tubulin, green). Nuclei were stained with DAPI (blue). White open boxes indicate the magnified images at the right. Arrows point to virus particle clumps detected by anti-VP7. The scale bar is 20 μm. (e–g) Plots from quantitative RT-PCR comparing rotavirus transcripts of NSP5, VP6, and housekeeping gene (SDHA) in noninfected (NI), rRV/wt- and rRV/VP4-BAP-infected cellular extracts at 4 hpi. The results correspond to the mean ± SEM of three independent experiments, ordinary one-way ANOVA; **, $P < 0.01$; ***, $P < 0.001$; ****, $P < 0.0001$.

compared to that of rRV/wt at short times after removing the drug (2 min), as confirmed by both a reduced ratio of cells presenting viroplasms (Fig. 7c) and a reduced number of viroplasm per cell (Fig. 7d). In order to further characterize the relationship between viroplasms and VP4, we performed transcriptional silencing experiments with VP4-specific siRNAs (siVP4) in MA/NSP2-mCherry cells (Fig. 7e). In this context, it has been previously described that the silencing of VP4 during RV infection leads to viroplasm formation even if TLPs assembly is impaired (60). We then monitored viroplasm formation in siVP4 and control-siRNA (scr) transfected MA104 cells, infected with simian strain SA11, and treated with 1,6-HD, as described for the experiment shown in Fig. 7a. The reassembly of the viroplasms in VP4-silenced cells had a delayed recovery kinetic similar to that observed for rRV/VP4-BAP viroplasms (Fig. 7f and g).
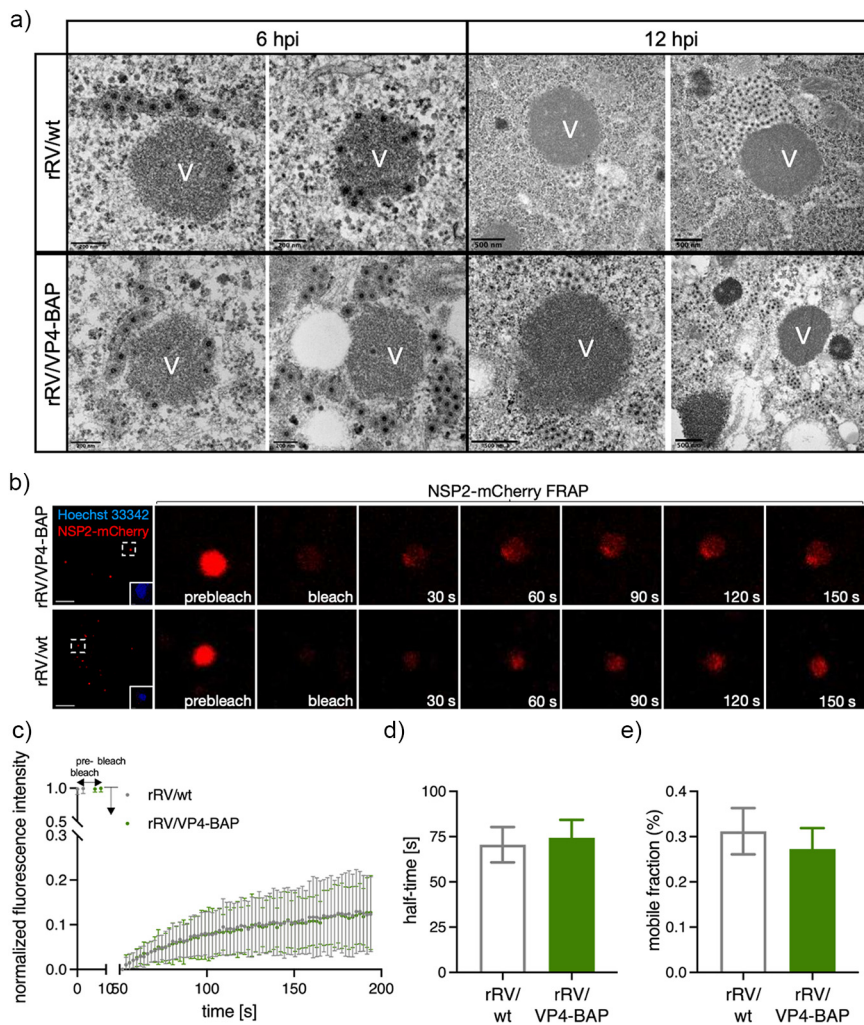
FIG 5 Viroplasm morphology and behavior for rRV/wt and rRV/VP4-BAP. (a) Representative high-resolution electron micrograph of viroplasms from rRV/wt (upper row) and rRV/VP4-BAP (lower row) infected MA104 cells at 6 hpi (left panel) and 12 hpi (right panel). Scale bars are 200 nm and 500 nm, as indicated. (b) Fluorescence images of FRAP measurement of single viroplasm of cells infected with rRV/VP4-BAP (top) and rRV/wt (bottom) at prebleach, postbleach, and recovery time conditions. Each inset indicates the bleached viroplasm of the images at the right. Nuclei were stained with Hoechst 33342. The scale bar is 10 μm. (c) FRAP recovery curve of NSP2-mCherry in single viroplasm from rRV/VP4-BAP (green) and rRV/wt (gray) infected MA/NSP2-mCherry cells at 5 hpi (n = 27 and 25, respectively). Plots indicating recovery half-time (d) and diffusion (e) means of NSP2-mCherry in single viroplasms of rRV/VP4-BAP and rRV/wt after photobleaching.

Furthermore, as in the case of rRV/VP4-BAP infection (Fig. 7d), the number of viroplasms per cell was significantly decreased in siVP4-treated cells at 2 min of recovery compared to the experimental controls (Fig. 7h). Thus, these results strongly suggest that VP4 promotes either indirectly or directly the assembly of viroplasms.

VP4-BAP impairs VLS assembly and association of actin filaments. Viroplasm-like structures (VLSs) are simplified models for the study of complex viroplasm structures, which require the coexpression of NSP5 with either NSP2 (24) or VP2 (22) to form globular cytosolic inclusions morphologically similar to viroplasms but unable to replicate and produce virus progeny. Considering this rationale, we formed VLSs by expressing NSP5 and NSP2 in the presence of GFP, VP4-GFP, or VP4-BAP-GFP (Fig. 8a). We noticed absence of colocalization of either VP4-GFP or VP4-BAP-GFP in VLSs. Furthermore, the number of VLSs per cell formed in the presence of VP4-GFP was much larger than that produced in the presence of VP4-BAP-GFP or GFP (Fig. 8b).
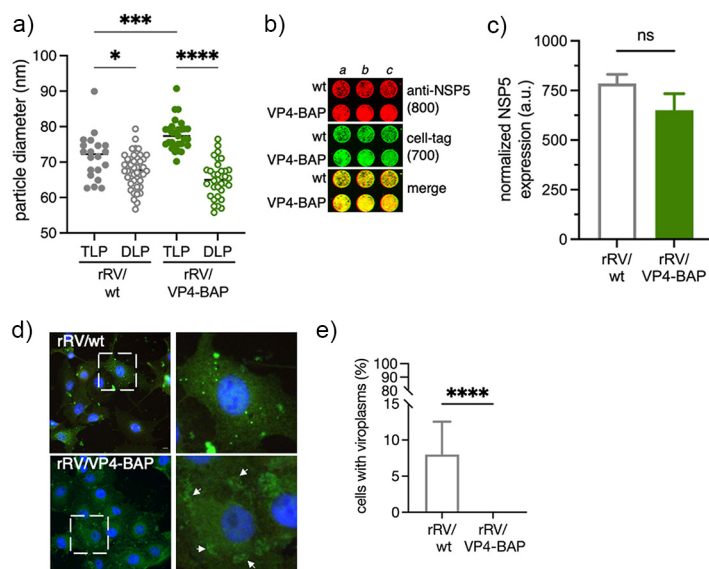
FIG 6 Transfection of rRV/VP4-BAP DLPs is inefficient in forming viroplasms. (a) Size plot of TLPs and DLPs purified from rRV/wt and rRV/VP4-BAP. The median value is indicated, $n > 30$ particles, ordinary one-way ANOVA; *, $P < 0.05$; ****, $P < 0.0001$. (b) In-cell Western blot of MA104 cells transfected for 4 h with identical numbers of rRV/wt and rRV/VP4-BAP DLPs. RV infection was detected by staining with anti-NSP5 (IDye800, red). The loading control corresponds to cell tag 700 (green). The merge of the two channels is shown at the bottom. (c) Plot showing normalized amounts of NSP5 in rRV/wt and rRV/VP4-BAP DLPs-transfected MA104 cells. Each experiment was done in triplicate. (d) Micrograph of rRV/wt and rRV/VP4-BAP DLPs-transfected MA104 cells immunostained to detect viroplasms with anti-NSP5 (green). Nuclei were stained with DAPI (blue). Open dashed white box shows enlarged viroplasm inset at the right. White arrowheads point to early-stage viroplasm structures. The scale bar is 10 μm. (e) Quantification of the cells showing viroplasms upon transfection with DLPs of rRV/wt and rRV/VP4-BAP. The data correspond to the mean $\pm$ SD, Welch's t test; ****, $P > 0.0001$.

Since VP4 associates with actin cytoskeleton components (45, 47, 48), we hypothesized that VP4-BAP-GFP could have an impaired association with actin filaments. To investigate this possibility, MA104 cells expressing VP4-GFP or VP4-BAP-GFP were untreated or treated with nocodazole for 1h before fixation. Nocodazole treatment induces depolymerization of the microtubule network, permitting direct characterization of proteins associated with the actin cytoskeleton. In this context (Fig. 8c), we stained cells to detect actin cytoskeleton and noticed that VP4-GFP was associated, as expected, with actin filaments even after nocodazole treatment, while VP4-BAP-GFP was associated with filaments only in the absence of nocodazole. In MT-depolymerized cells, VP4-BAP-GFP formed diffuse small cytosolic aggregates or short filaments. Moreover, while the length of VP4-GFP fibers was comparable in the presence or absence of nocodazole treatment, the VP4-BAP-GFP fibers were significantly shorter in cells treated with nocodazole (Fig. 8d), suggesting an impaired association of VP4-BAP with actin filaments. Taken together, these results suggest that VP4 promotes the assembly of VLSs mediated by its association with actin filaments.

Impaired association between the actin cytoskeleton and rRV/VP4-BAP results in delayed viroplasm assembly. RV strain SA11 infection (Fig. 9a and references 25 and 61) reorganizes the actin cytoskeleton, mainly by decreasing the actin stress fiber and redistributing it to the cell cortex. However, this reorganization did not take place in cells infected with rRV/VP4-BAP (Fig. 9b and Fig. S3a posted at https://zenodo.org/record/6865927#.YtfEH-xBw-Q), featured by an increment in stress fibers surrounding the viroplasms (Fig. 9b, yellow open arrows) and contrasted by an actin cell cortex increment in rRV/wt-infected cells. Moreover, the actin cytoskeleton was not properly reorganized even in experiments with an increased rRV/VP4-BAP multiplicity of infection (Fig. S3b at the URL mentioned above). Interestingly, the MT-network reorganization was attained by both viruses.
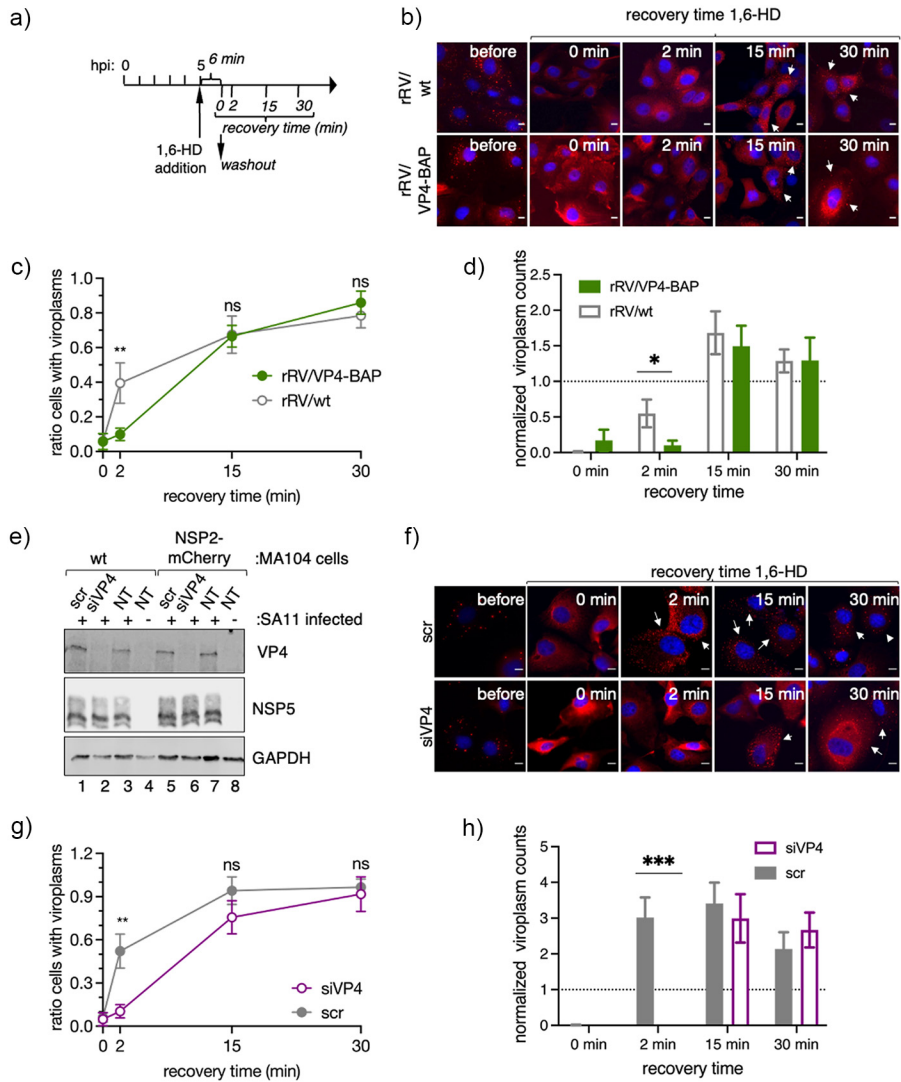
FIG 7 VP4 has a role in viroplasm formation. (a) Schematic representation for the characterization of LLPS condensates in viroplasms of RV-infected cells. At 5 hpi, RV-infected MA/NSP2-mCherry cells were treated with 1,6-HD for 6 min. The drug was washed out, and samples were fixed and imaged for viroplasm quantification at 0, 2, 15, and 30 min postrecovery. (b) Representative images of MA/NSP2-mCherry cells infected at 5 hpi with rRV/wt (upper row) or rRV/VP4-BAP (lower row) and treated with 3.5% of 1,6-HD. Cells were washed and monitored for viroplasm formation at 0, 2, 15, and 30 min postrecovery. White arrows point to cells with recovered viroplasms. The scale bar is 10 μm. Plots indicating the ratio of cells with viroplasms (c) and viroplasm counts per cell (d) normalized at initial conditions (5 hpi). Data represent the mean $\pm$ SEM of three independent experiments. Student's t test; **, $P < 0.001$. (e) Immunoblot of cellular extracts prepared at 6 hpi from noninfected or SA11-infected MA104 or MA/NSP2-mCherry cells silenced with siVP4 or control siRNA (scr). The membrane was stained with anti-VP4, anti-NSP5, and anti-GAPDH (loading control). (f) Representative images of SA11-infected MA/NSP2-mCherry cells knocked down with scr (upper row) or siVP4 (lower row) and treated for 6 min with 3.5% of 1,6-HD. Cells were washed and monitored for viroplasm formation at 0, 2, 15, and 30 min postrecovery. White arrows point to cells showing recovered viroplasms. The scale bar is 10 μm. Plot indicating the ratio of cells with viroplasms (g) and viroplasm counts per cell (h) normalized to initial conditions after recovery from 1,6-HD treatment of SA11-infected MA104 cells silenced with siVP4 or scr. The data represent the mean $\pm$ SEM. Student's t test; *, $P < 0.05$; ***, $P < 0.001$.

The cell contractility is regulated partly by the reorganization of stress fibers composed of actin and myosin II. Therefore, we questioned if the molecular motor myosin was also required for viroplasm assembly and if its activity was impaired in rRV/VP4-BAP infected cells. For this purpose, we inspected the localization of paralog myosin IIa in cells infected with either rRV/wt or rRV/VP4-BAP at 6 hpi and compared it with
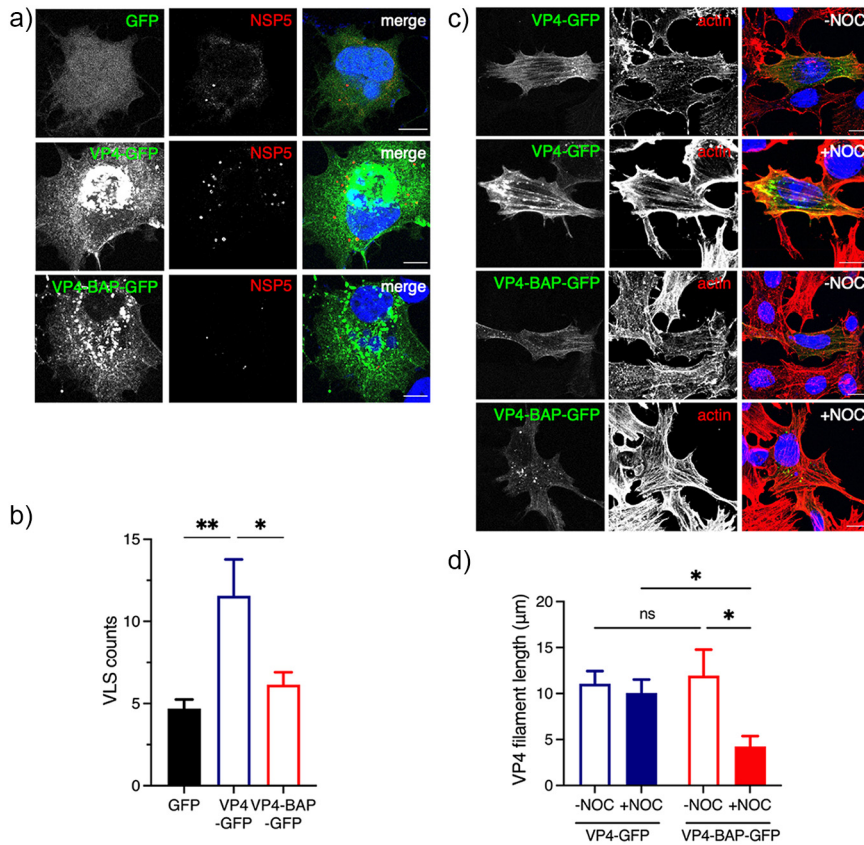
FIG 8 VP4-BAP does not bind to the actin cytoskeleton. (a) Immunostaining of MA104 cells showing NSP5 and NSP2 VLSs coexpressed with GFP (top panel), VP4-GFP (middle panel), and VP4-BAP-GFP (bottom panel). Cells were fixed with paraformaldehyde and immunostained to detect VLSs (anti-NSP5, red). Nuclei were stained with DAPI (blue). The scale bar is 10 μm. (b) Plot indicating the number of VLSs per cell when coexpressed with GFP, VP4-GFP, and VP4-BAP-GFP. The data represent the mean $\pm$ SEM, one-way ANOVA; *, $P < 0.05$; **, $P < 0.001$. (c) Immunostaining of MA104 cells expressing VP4-GFP and VP4-BAP-GFP after treatment for 1 h before fixation without (–NOC) or with (+NOC) 10 μM nocodazole. Cells were fixed with methanol at 24 hours posttransfection (hpt) and immunostained for GFP detection (anti-GFP, green) and actin cytoskeleton (anti-actin, red). Nuclei were stained with DAPI (blue). The scale bar is 10 μm. (d) Plot for the quantification of VP4-GFP and VP4-BAP-GFP filament lengths associated with actin filaments in cells untreated or treated with nocodazole. The data represent the mean$\pm$ SD, Welch's t test: ****, $P < 0.0001$.

noninfected conditions (Fig. 9c). In noninfected cells, myosin IIa is homogenously distributed in filaments, stacks, clusters, and continuous structures (62). However, upon rRV/wt infection, continuous myosin structures are lost, and myosin clusters and stacks in the cell cortex are favored (Fig. 9c, yellow open arrowheads). In contrast, rRV/VP4-BAP-infected cells still have continuous structures, mainly in the cellular ventral region. Interestingly, VP4 fibrillar morphology is observed in rRV/wt-infected cells (Fig. 9b and c, red open arrows) but not in rRV/VP4-BAP-infected cells.

We confirmed the active role of the actin cytoskeleton in the assembly of rRV/wt and rRV/VP4-BAP viroplasms by adding actin inhibitors jasplakinolide (jasp) and cytochalasin B (cyt B) at 1 hpi, a time in which virus internalization and primary virus transcription are well initiated (Fig. 9d). In this context, we noted that rRV/wt viroplasms were sensitive to jasp and cyt B treatment, as the ratio of cells showing viroplasms (Fig. 9e) and the number of viroplasms per cell (Fig. 9f) were significantly decreased, reaching the levels observed in rRV/VP4-BAP-infected cells in presence or absence of actin inhibitors.

We next inhibited the nonmuscular myosin II using blebbistatin (BLB) (63), a small molecule inhibiting both myosin II paralogs a and b (Fig. 9g to i). Like the actin inhibitors, blebbistatin reduced the ratio of cells with viroplasms (Fig. 9h) and the number of viroplasms
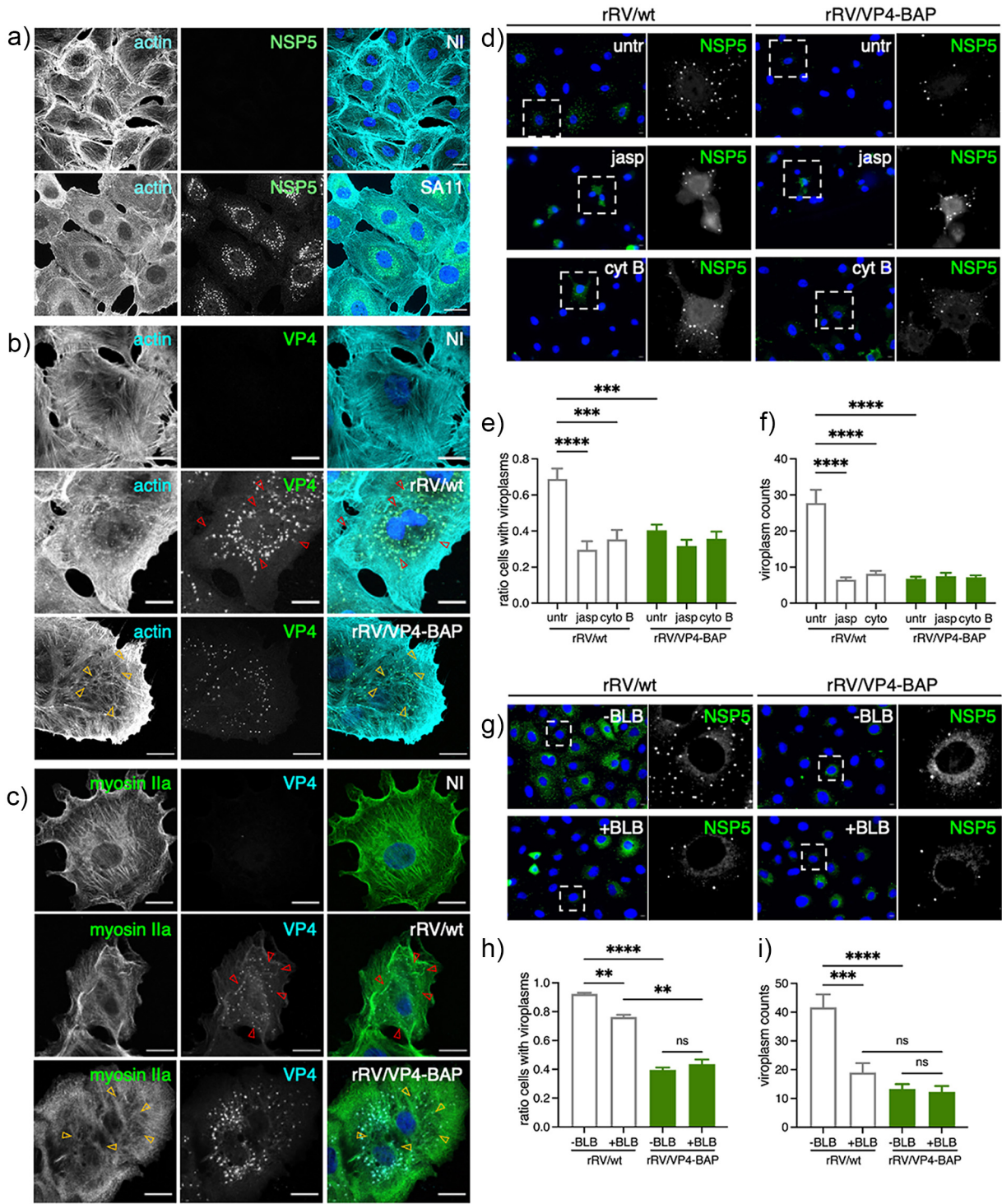
FIG 9 rRV/VP4-BAP impaired association with the actin cytoskeleton. (a) Immunostaining of noninfected and SA11-infected MA104 cells. At 6 hpi, cells were fixed with methanol and immunostained to detect viroplasms (anti-NSP5, green) and actin cytoskeleton (anti-actin, cyan). Nuclei were stained with DAPI (blue). The scale bar is 20 μm. Immunostaining of noninfected and rRV/wt- or rRV/VP4-BAP-infected MA104 cells. At 6 hpi, cells were fixed with methanol and immunostained for detection of (b) VP4 (anti-VP4, green) and actin cytoskeleton (anti-actin, cyan) and (c) VP4 (anti-VP5 clone 4G2, cyan) and myosin motor (anti-myosin IIa, green). Nuclei were stained with DAPI (blue). The scale bar is 20 μm. Open yellow and red arrowheads point to stress fibers in the actin cytoskeleton and VP4 fibers, respectively. (d) Immunofluorescence of rRV/wt and rRV/VP4-BAP-infected MA104 cells treated at 1 hpi with either 0.5 μM jasplakinolide (jasp; middle panel) or 10 μM cytochalasin B (cyt B; lower panel). At 6 hpi, cells were fixed and immunostained to detect viroplasms (anti-NSP5, green). Nuclei were stained with DAPI (blue). The dashed open box corresponds to the inset of the enlarged image at the right. The scale bar is 10 μm. Plot for the quantification of (e) the ratio of cells showing viroplasms and (f) the number of viroplasms per cell. (g) Immunofluorescence of rRV/wt- and rRV/VP4-BAP-infected MA104 cells untreated or treated at 1 hpi with 5 μM blebbistatin (BLB). At 6 hpi, cells were fixed and immunostained to detect viroplasms (anti-NSP5, green). Nuclei were stained with DAPI (blue). The dashed open box is an inset of the enlarged image at the right. The scale bar is 10 μm. Plot for the quantification of (h) the ratio of cells showing viroplasms and (i) the number of viroplasms per cell.
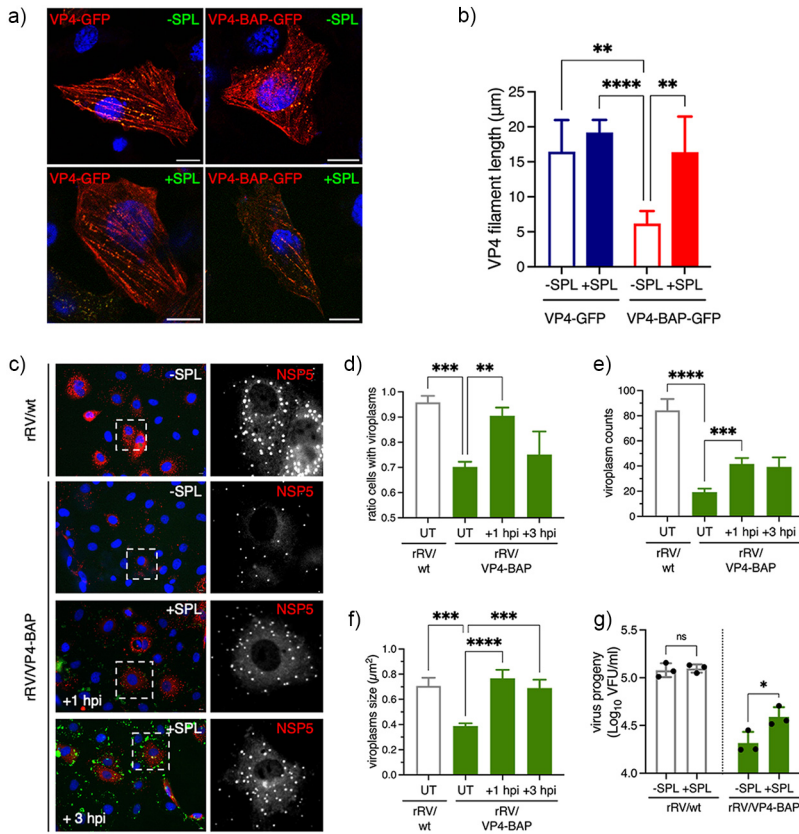
FIG 10 A peptide mimicking loop K145-G150 rescues the rRV/VP4-BAP phenotype. (a) Immunofluorescence images at 17 hpt of BHK-T$_7$ cells expressing VP4-GFP or VP4-BAP-GFP, untreated or treated with 25 μM SPL added immediately after transfection. Before methanol fixation, cells were treated for 1 h with 10 μM nocodazole. The cells were immunostained for GFP (anti-GFP, red), and nuclei were stained with DAPI (blue). Scale bar is 10 μm. (b) Plot quantifying the length of VP4 filaments untreated or treated with SPL as described in panel a. Welch ANOVA test; **, $P < 0.01$; ****, $P < 0.0001$. (c) Representative immunofluorescence microphotograph of viroplasms of rRV/wt- and rRV/VP4-BAP-infected cells untreated (-SPL) or treated (+SPL) at +1 and +3 hpi with 25 μM SPL, as indicated. Viroplasms were immunostained at 6 hpi with anti-NSP5 (red), and nuclei were stained with DAPI (blue). The dashed white boxes correspond to the enlarged picture in the right columns. Scale bar is 10 μm. Quantification plots for the ratio of cells with viroplasms (d) and the numbers (e) and size (f) of viroplasms per cell of MA104 cells infected with the indicated virus and untreated (UT) or treated with 25 μM SPL at +1 and +3 hpi. The data represent the mean $\pm$ SEM using Welch's ANOVA test; ***, $P < 0.001$; ****, $P < 0.0001$. (g) Plot determining the virus progeny of rRV/wt- and rRV/BAP-infected cells untreated or treated at 1 hpi with 25 μM SPL. The data represent the mean +SEM of three independent experiments. Welch's ANOVA test; *, $P < 0.05$.

per cell (Fig. 9i) in cells infected with rRV/wt but not with rRV/VP4-BAP. Our results suggest that viroplasm assembly requires actin and myosin II in a mechanism involving VP4.

A small peptide mimicking loop K145-G150 rescues the rRV/VP4-BAP phenotype. It has been described that the C-terminal region of VP5* harbors an actin-binding domain (45). We hypothesize that the insertion of a BAP tag in the loop K145-G150 interferes with VP5* and actin-cytoskeleton association, resulting in a delay in viroplasm assembly. To prove this hypothesis, we designed a small peptide harboring the amino acid sequence from V143 to G156 of wt VP4 comprising loop K145-G150, flanked at the N-terminus by an arginine tail and at the C-terminus by conjugation to fluorescein isothiocyanate (FITC), for peptidic internalization and visualization, respectively. Thus, the sequence of this small peptide corresponds to RRRRRR^{143}VV^{145}KTTANG^{150}SIGQYG^{156}-FITC, and was designated <u>s</u>mall <u>p</u>eptide <u>l</u>oop K145-G156 (SPL). Of note, SPL was not toxic for cells up to a concentration of 100 μM even after 24 h of treatment (Fig. S4a posted at https://zenodo.org/record/6865927#.YtfEH-xBw-Q). SPL was internalized in cells at 2 h posttreatment and found diffuse in the cytosol (Fig. S4b at the URL mentioned above). First (Fig. 10a), we

expressed VP4-GFP and VP4-BAP-GFP (stained with anti-GFP, red) in BHK-T$_7$ cells in the absence or presence of SPL and monitored the filamentous distribution of these proteins. Interestingly, as quantified in Fig. 10b, the addition of SPL increased the length of VP4-BAP-GFP filaments compared to the untreated sample, reaching the same level of the fiber lengths as VP4-GFP. The filamentous distribution of VP4-GFP did not change with SPL treatment. We next investigated if SPL can improve the replication fitness of rRV/VP4-BAP. For this, SPL was added at 1 or 3 hpi to MA104 cells infected with either rRV/wt or rRV/VP4-BAP and then monitored at 6 hpi for viroplasm formation (Fig. 10c). Interestingly, the addition of SPL at 1 hpi drastically improved the number of cells presenting viroplasms in rRV/VP4-BAP-infected cells, reaching similar levels as observed in rRV/wt-infected cells (Fig. 10d). Consistently, the viroplasm size and numbers per cell increased upon SPL treatment at 1 hpi (Fig. 10e and f). The addition of SPL at 3 hpi increased the viroplasm size but did not increase the number of viroplasms per cell. The treatment of rRV/wt-infected cells with SPL did not affect viroplasm size and numbers (Fig. S5c–d at the URL mentioned above). We then tested the ability of SPL to rescue rRV/VP4-BAP virus progeny. For this purpose, rRV/VP4-BAP-infected cells were treated at 1 hpi with SPL, and virus progeny was recovered at 12 hpi. As shown in Fig. 10g, rRV/VP4-BAP virus progeny formation significantly increased upon treatment with SPL, while the same treatment had no effect on rRV/wt progeny formation. We concluded that SPL boosted the association of VP4-BAP with actin-bundles, thereby rescuing the assembly of viroplasms with a concomitant increase in the production of virus progeny.

DISCUSSION

The external coat layer of the RV virion can be modified *in vitro* by adding a specific ratio of VP7 and VP4 proteins to purified DLPs to generate recoated TLPs (rcTLPs) (10–12, 64). This approach provides a valuable tool for studying the VP4 structural requirements for virion internalization (10). However, rcTLPs have methodological limitations and do not allow transferring the parental phenotype to the virus progeny. Moreover, rcTLPs only allow single amino acid substitutions in the VP4 spike protein (65, 66). However, the recently implemented entirely plasmid-based RV reverse genetics technology resulted in a valuable tool for studying several aspects of RV replication and the development of future RV-based vaccines. Specifically, RV reverse genetics technology has demonstrated that gs4, encoding VP4, can be artificially reassorted or recombined by transferring human RV strain gs4 into a simian strain SA11 backbone (54).

In the present study, we used an RV reverse genetics system to remodel the spike protein VP4 by incorporating a BAP tag in four independent exposed loops in the VP8* lectin domain. Interestingly, although the four differently modified proteins were efficiently biotinylated when expressed alone in transfected cells, only one harboring a BAP tag inserted in the K145-G150 loop, termed rRV/VP4-BAP, was rescued using RV reverse genetics (54). We hypothesize that those VP4-BAP versions, which were unable to be rescued, could have strongly compromised their virus progeny because they directly impacted, as shown by *in silico* modeling of these structures (Fig. S5a posted at https://zenodo.org/record/6865927#.YtfEH-xBw-Q), (i) the VP4 transition states from upright (immature) to reverse (mature) (65), (ii) the VP4 association with specific cellular receptors (36, 37), or (iii) the incorporation of VP4 in the coat layer.

VP4-BAP and VP4 share similar distribution patterns in infected cells, such as their localization surrounding viroplasm and the endoplasmic reticulum in colocalization with VP7, and incorporation into newly assembled virions. However, we found that rRV/VP4-BAP had a significantly reduced replication fitness compared to rRV/wt, which correlates with a reduced number of rRV/VP4-BAP viroplasm per cell. To identify the reason for this, we investigated the various steps involved in RV replication. We show that rRV/VP4-BAP internalization kinetics are comparable to rRV/wt. This internalization kinetics consists of a sequence of events starting with the interaction of the virus with the cell membrane and concluding with the decrease of calcium levels within the endosomes, provoking the loss of the outer layer of the virion, which triggers the

release of transcriptionally active DLPs into the cytosol (66–69). We also confirmed that virus transcription and translation are comparable between both viruses. Moreover, there were no differences in rRV/VP4-BAP viroplasm morphology and liquidlike dynamics, as determined by high-resolution electron microscopy and NSP2-mCherry mobility in single-viroplasm FRAP experiments, respectively. However, upon transfection with rRV/VP4-BAP, DLPs that bypass the virus physiological internalization pathway showed a delayed viroplasm formation compared with rRV/wt DLPs, even though NSP5 expression levels were equivalent for both viruses. Collectively, these results indicate that the reduced replication fitness of rRV/VP4-BAP is due to a step between primary virus translation and viroplasm formation. We hypothesized that rRV/VP4-BAP, and specifically VP4-BAP, was defective in associating with the actin cytoskeleton because of (i) a delayed recovery of rRV/VP4-BAP viroplasms after 1,6-HD treatment, (ii) inability of VP4-BAP-GFP to increase the VLS counts, (iii) absence of colocalization of VP4-BAP-GFP with actin stress fibers, (iv) inability of rRV/VP4-BAP to reorganize actin cytoskeleton, and (v) insensitivity of rRV/VP4-BAP viroplasms for drugs depolymerizing actin filaments and inhibiting myosin II molecular motor. In contrast, rRV/wt infection led to the reorganization of the actin cytoskeleton, and rRV/wt viroplasms were sensitive to actin-depolymerizing and myosin inhibitor drugs linking actin with viroplasm assembly. Additionally, the numbers of VLSs duplicated when coexpressed with VP4-GFP. Previous studies (45, 49) demonstrated the ability of VP4 to associate with actin in the absence of other virus proteins, mainly through an actin-binding domain present in the C-terminal region of VP5* (residues 713–776) when in cooperation with the coiled-coil domain (residues 481–574). In this context, we also present evidence that the sole expression of VP4 allows its association with actin. Importantly, by employing rRV/VP4-BAP infection, we show that the association of VP4 with actin is essential to catalyze the formation of viroplasms. This finding provides an additional function to VP4 in RV replication.

Interestingly, incorporating a small peptide mimicking loop V143-G156 of VP4 during rRV/VP4-BAP infection reverted the impaired formation of viroplasm with a significant improvement in virus progeny production. We concluded that rRV/VP4-BAP replication is enhanced because SPL raised the association of actin with VP4-BAP during virus infection and because we observed that VP4-BAP, in the absence of other viral proteins, associated with actin filament when expressed with SPL. Interestingly, an increased concentration of SPL enhances actin expression but not VP5 (Fig. S6 posted at https://zenodo.org/record/6865927#.YtfEH-xBw-Q), which can be associated with an improvement in cell motility (70). It is therefore possible that the VP8* subunit promotes viroplasm assembly and stabilization through at least one of these three aspects: (i) association of VP8* with a yet-undescribed host component, (ii) reorganization of VP5*–VP8* association, or (iii) a direct role of VP8* over another RV protein in viroplasm assembly. The role of the actin cytoskeleton in the RV life cycle, particularly internalization and egress, has been previously demonstrated (39, 47, 71). Here, we show that the actin cytoskeleton is also involved in viroplasm formation, an essential intermediate stage of RV replication. Furthermore, it has been described that the silencing of Rac1, a member of the Rho family of small GTPases playing a major role in actin- and microtubule-cytoskeleton dynamics, leads to a decrease in RV progeny formation in a process downstream of cell entry (71). We therefore cannot exclude activation of Rac1 by VP4, allowing reorganization of the actin cytoskeleton for an efficient assembly of the viroplasms.

Finally, specific *in vivo* biotinylation of cellular targets can be achieved by adding a BAP tag to the protein of interest and coexpressed with the *E.coli*-derived biotin ligase, BirA (72). This method is a powerful tool for versatile applications, such as identifying highly complex interactomes (73, 74), and permits batch protein and subviral particle (51, 52) refinement at high purity and in physiological conditions. Incorporating a BAP tag in RV VP6 allowed the preparation and purification of replication-competent DLPs (52). Identifying a permissive target site in loop K145-G150 of VP4 spike protein for the insertion of an exogenous peptide may impact the RV field. This VP4 modification

favors the insertion of peptides required for super-resolution microscopy or DNA-paint technologies (e.g., Halo or BC2 tags) to dissect debated aspects of RV entry. In addition, this VP4 modification technology could permit the incorporation of antigenic peptides for vaccine development. Although it is well known that the current oral RV vaccines elicit an efficient immune response (75, 76), rRV harboring a modified VP4 could provide an improved vaccination platform for the display of other antigens fostering the development of a new generation of dual vaccines.

MATERIALS AND METHODS

Cells and viruses. MA104 cells (embryonic African green monkey kidney cells; ATCC CRL-2378) were grown in Dulbecco's modified Eagle's medium (DMEM) (Life Technologies) containing 10% fetal calf serum (FCS) (AMIMED; BioConcept, Switzerland) and penicillin (100 U/mL)–streptomycin (100 μg/mL) (Gibco, Life Technologies). MA/cytBirA and MA/NSP2-mCherry (59) cell lines were grown in DMEM supplemented with 10% FCS, penicillin (100 U/mL)-streptomycin (100 μg/mL), and 5 μg/mL puromycin (InvivoGen, France). BHK-T$_{7/9}$ (baby hamster kidney stably expressing T$_7$ RNA polymerase) cells were kindly provided by Naoto Ito (Gifu University, Japan) (77) and cultured in Glasgow medium supplemented with 5% FCS, 10% tryptose phosphate broth (Sigma-Aldrich), 10% FCS, penicillin (100 U/mL)-streptomycin (100 μg/mL), 2% nonessential amino acids, and 1% glutamine.

rRV/wt (59), rRV/VP4-BAP, and simian rotavirus strain SA11 (G3P6[1]) (78) were propagated, grown, and purified as previously described (79). Virus titer was determined as viroplasm-forming units per mL (VFU/mL) as described by Eichwald et al. (2012) (25). The T$_7$ RNA polymerase recombinant vaccinia virus (strain vvT7.3) was amplified as previously described (80).

Cell line generation. MA/cyt-BirA cell line was generated using the PiggyBac technology (81). Briefly, 1×10^5 MA104 cells were transfected with the pCMV-HyPBase (81) and transposon plasmids pPB-cytBirA using a ratio of 1:2.5 with Lipofectamine 3000 transfection reagent (Invitrogen, Thermo Fisher Scientific) according to the manufacturer's instructions. The cells were maintained in DMEM supplemented with 10% FCS for three days and then selected for 4 days in DMEM supplemented with 10% FCS and 5 μg/mL puromycin (59).

Reverse genetics. rRV/VP4-BAP was prepared as described previously (59, 82) using a pT$_7$-VP4-BAP instead of pT$_7$-VP4. Briefly, monolayers of BHK-T$_7$ cells (4×10^5) cultured in 12-well plates were cotransfected using 2.5 μL of TransIT-LT1 transfection reagent (Mirus) per microgram of DNA plasmid. The mixture comprised 0.8 μg of SA11 rescue plasmids (pT$_7$-VP1, pT$_7$-VP2, pT$_7$-VP3, pT$_7$-VP4-BAP, pT$_7$-VP6, pT$_7$-VP7, pT$_7$-NSP1, pT$_7$-NSP3, and pT$_7$-NSP4) and 2.4 μg of pT$_7$-NSP2 and pT$_7$-NSP5 (83, 84). Additionally, 0.8 μg of pcDNA3-NSP2 and 0.8 μg of pcDNA3-NSP5, encoding NSP2 and NSP5 proteins, were cotransfected to increase rescue efficiency (59, 82). Next, cells were cocultured with MA104 cells for 3 days in serum-free DMEM supplemented with trypsin from porcine pancreas (0.5 μg/mL final concentration) (T0303, Sigma-Aldrich) and lysed by freeze-thawing. Then, 300 μL of the lysate was transferred to new MA104 cells and cultured at 37°C for 4 days in serum-free DMEM supplemented with 0.5 μg/mL trypsin until a visible cytopathic effect was observed. The modified genome segments of rescued recombinant rotaviruses were confirmed by specific PCR segment amplification followed by sequencing (59).

Antibodies and chemicals. Guinea pig anti-NSP5, guinea pig anti-RV, goat anti-RV, mouse monoclonal anti-NSP5 (clone 2D2), and rabbit anti-VP4 were described previously (25, 85–88). Mouse monoclonal anti-VP5 (clone 2G4) and mouse monoclonal anti-VP7 (clone 159) were kindly provided by Harry Greenberg (Stanford University, CA, USA). Rabbit anti-simian rotavirus VP4 was purchased from Abcam. Mouse MAb anti-glyceraldehyde dehydrogenase (GAPDH) (clone GAPDH-71.1), mouse anti-alpha tubulin (clone B-5-1-12), and mouse MAb anti-β-actin (clone AC-74) were purchased from Merck. Mouse MAb anti-GFP clone (C-2) was purchased from Santa Cruz Biotechnology, Inc. Mouse MAb anti-α-tubulin was directly conjugated to Atto 488 using the Lightning-Link Atto 488 conjugation kit from Innova Bioscience, United Kingdom. Streptavidin-HRP was purchased from Merck. Streptavidin-Alexa 555 and secondary antibodies conjugated to Alexa 488, Alexa 594, Alexa 647, Alexa 700 were purchased from ThermoFisher Scientific.

1,6-hexanediol, nocodazole, jasplakinolide, and cytochalasin B were purchased from Merck. (-)-Blesbbistatin was purchased from Cayman Chemical, USA.

Amino acids and their derivatives were purchased from Advanced ChemTech, Novabiochem, Iris Biotech GMBH, Sigma-Aldrich, PolyPeptide, Space Peptides, and GL BioChem. Amino acids were used as the derivatives Fmoc-Arg(Pbf)-OH, Fmoc-Leu-OH, Fmoc-Lys(Boc)-OH, Fmoc-Lys(Fmoc)-OH, Fmoc-Pro-OH, Fmoc-Val-OH, Fmoc-Trp(Boc)-OH, Fmoc-Ile-OH, Fmoc-Gln(Trt)-OH, Fmoc-Tyr(tBu)-OH, Fmoc-Ala-OH, and Rink Amide AM resin (loading: 0.38 mmol·g^{-1}) and were purchased from Sigma-Aldrich. OxymaPure (hydroxyiminocyanoacetic acid ethyl ester) and DIC (N,N'-diisopropylcarbodiimide) were purchased from Iris Biotech GMBH. 5(6)-carboxyfluorescein (CF) was from Sigma. EM104 10-mL glass syringes were from Sanitex International.

DNA plasmids. pcDNA-VP4-SA11 was obtained by RT-PCR amplification of VP4 ORF of gs4 of simian rotavirus strain SA11 (89) using specific primers to insert HindIII and XhoI sites, followed by ligation into those sites in pcDNA3 (Invitrogen). pcDNA-VP4-KpnI/BamHI was built by insertion of point mutations in pcDNA-VP4-SA11 using the QuikChange site-directed mutagenesis kit and protocol (Agilent) to insert KpnI and BamHI restriction sites in VP4. pcDNA-VP4-BAP was obtained by ligation between KpnI and BamHI of pcDNA-VP4-KpnI/BamHI, a synthetic DNA fragment (GenScript) containing a BAP tag in VP4

loops in amino acid regions 96–101 (blue), 109-114 (orange), 132–137 (pink), and 145–150 (green). The BAP tags are flanked by BspEI and NheI restriction sites for easy tag replacement.

RV plasmids pT_7-VP1-SA11, pT_7-VP2-SA11, pT_7-VP3-SA11, pT_7-VP4-SA11, pT_7-VP6-SA11, pT_7-VP7-SA11, pT_7-NSP1-SA11, pT_7-NSP2-SA11, pT_7-NSP3-SA11, pT_7-NSP4-SA11, and pT_7-NSP5-SA11 were previously described (83). pcDNA3-NSP5 and pcDNA3-NSP2 were already described (59). pT_7-VP4-BAP (blue), (orange), (green), and (pink), assigned as described above, were obtained by inserting a synthetic DNA fragment (Genscript) encoding for the VP4 protein-encoding BAP tag flanked by MfeI and NdeI restriction enzymes sites and ligated into those sites in the pT_7-VP4-SA11.

pPB-cytBirA was obtained from a synthetic DNA fragment (Genscript) containing the BirA enzyme open reading frame of *Escherichia coli* (UniProt accession number: P06709) (90) and inserted in the pPB-MCS vector (82) using NheI-BamHI restriction enzymes sites.

pcDNA-NSP5(SA11) and pcDNA-NSP2(SA11) were previously described (24, 91). pCI-VP4-GFP and pCI-VP4-BAP plasmids were obtained from PCR amplification of pT_7-VP4-SA11 and pT_7-VP4-BAP (green) using specific primers to insert NheI and MluI sites, followed by ligation in-frame on those sites in pCI-GFP. Thus, the GFP fragment was PCR amplified from pEGFP-N1 (Clontech) using specific primers to insert MluI/NotI restriction enzyme sites and ligated on those restriction enzyme sites into pCI-Neo (Promega). All of the oligonucleotides were obtained from Microsynth AG, Switzerland. A list of all DNA sequences synthesized is provided in Table S1 posted at https://zenodo.org/record/6865927#.YtfEH-xBw-Q.

Streptavidin-supershift assay and immunoblotting. The assay was performed as described by Predonzani et al. (51). Briefly, cell extracts were lysed in TNN lysis buffer (100 mM Tri-HCl pH 8.0, 250 mM NaCl, 0.5% NP-40, and cOmplete Protease Inhibitor [Roche]) and centrifuged for 7 min at 15,000 rpm and 4°C. The supernatant was exhaustively dialyzed against PBS (phosphate-buffered saline, 137 mM NaCl, 2.7 mM KCl, 8 mM Na_2HPO_4, and 2 mM KH_2PO_4 pH 7.2) at 4°C and heated for 5 min at 95°C in Laemmli sample buffer. Samples were incubated for 1 h at 4°C with 1 μg streptavidin (Sigma) and then resolved in SDS-polyacrylamide gel under reducing conditions. Proteins were transferred to nitrocellulose 0.45 μm (92) and incubated with corresponding primary and secondary antibodies. Secondary antibodies were conjugated to IRDye680RD or IRDye800RD (LI-COR, Germany) for protein detection and quantification in Odyssey Fc (LI-COR Biosciences). The percentage of biotinylated proteins is determined according to the following formula:

$$\%biotinylated\ protein = \left[\frac{intensity\ unbiotinylated\ sample - intensity\ biotinylated\ sample}{intensity\ unbiotinylated\ sample}\right]/100$$

The intensity of both unbiotinylated and biotinylated samples corresponds to the unshifted band. The intensity was measured using Image Studio Acquisition Software, LI-COR version (5.2.5).

Virus fitness curve. The experiment was performed as described previously (93) with some modifications. MA104 cells (1 $\times$ 10^5) seeded in 24-well plates were infected with rRV at an MOI of 10 VFU/cell. The virus was allowed to adsorb for 1 h at 4°C, followed by incubation at 37°C in 500 μL DMEM. At the indicated time points, the plates were frozen at −80°C. Each time point was performed in triplicate. The cells were freeze-thawed for three cycles, harvested, and centrifuged at 900 $\times$ *g* for 5 min at 4°C. The supernatant was recovered and activated with 80 μg/mL of trypsin for 30 min at 37°C. Two-fold serial dilutions were prepared and used to determine the viral titers described previously (59, 82).

Fluorescence labeling of purified rRV. 100 μL of purified and trypsin-activated biotinylated rRV/VP4-BAP was incubated with 1 μL of streptavidin-Alexa Fluor 555 (2 mg/mL) (ThermoFisher Scientific) for 1 h at room temperature. The tube was snaped every 20 min. Unbound streptavidin and streptavidin conjugated to rRV/VP4-BAP were separated by loading the 50 μL reaction mixture on top of 100 μL of a 20% sucrose-PBS cushion followed by centrifugation for 40 min at 20 lb/in^2 in an air-driven ultracentrifuge (Airfuge, Beckman Coulter). Pellet was resuspended in 20 μL TBS (25 mM Tris-HCl, pH 7.4, 137 mM NaCl, 5 mM KCl, 1 mM $MgCl_2$, 0.7 mM $CaCl_2$, 0.7 mM Na_2HPO_4, 5.5 mM dextrose).

Immunofluorescence. For virus internalization experiments, 1 μL of rRV particles conjugated to StAV-Alexa555 diluted in 50 μL of DMEM was adsorbed over MA104 cells for 15 min and kept on a metal tray cooled to −20°C. Cells were then transferred to 37°C and fixed at the indicated time points with ice-cold methanol for 3 min on dry ice.

For later times postinfection, the virus was adsorbed for 1 h at 4°C in a reduced volume. Then, cells were transferred to 37°C and treated at the indicated time points with 100 μM biotin in serum-free DMEM. Cells were fixed when indicated in 2% paraformaldehyde in phosphate-buffered saline (PBS) for 10 min at room temperature or in ice cold-methanol for 3 min at −20°C.

VLS experiments were performed as described by Buttafuoco et al. (92). In experiments using the inhibitors, the drug was added at 1 hpi and maintained until 6 hpi. The concentrations used 0.5 μM jasplakinolide (61, 71), 10 μM cytochalasin B (94), and 5 μM blebbistatin (63), as described elsewhere.

All immunofluorescence assays were processed as described by Buttafuoco et al. (92). Images were acquired using a confocal laser scanning microscope (CLSM) (DM550Q; Leica). Data were analyzed with the Leica Application Suite (Mannheim, Germany) and Image J (95).

LLPS assay. MA/NSP2-mCherry cells were seeded at a density of 1.2 $\times$ 10^4 cells per well in 8-well Lab-Tek Chamber Slides (Nunc Inc., Cat #177402). For RV infection, the virus was adsorbed at MOI of 25 VFU/cell diluted in 30 μL of serum-free DMEM, incubated at 4°C for 1 h in an orbital shaker, and then volume filled to 100 μL with serum-free DMEM followed by incubation at 37°C. At 5 hpi, the medium was replaced by medium containing 3.5% 1,6-hexanediol in 2% FCS-DMEM and cells were incubated for 6 min at 37°C. Then the drug was washed out by removing the medium, washing the cells three times with PBS, adding fresh 2% FCS-DMEM, and incubating at 37°C. At the designated time postrecovery, cells were fixed with 2% PFA for 10 min at room temperature. Finally, nuclei were stained by incubating cells

with 1 μg/mL of DAPI (4',6-diamidino-2-phenylindole) in PBS for 15 min at room temperature. Samples were mounted in ProLong Gold antifade mountant (ThermoFisher Scientific), and images were acquired using a fluorescence microscope (DMI6000B, Leica). Data were analyzed using ImageJ software (version 2.1.0/1.53; https://imagej.net/Fiji).

Quantification of viroplasms. The number of viroplasms was acquired and analyzed as previously described (25, 61, 94). Data analysis was performed using Microsoft Excel for Mac version 16.58. Statistical analysis, unpaired parametric Welch's t test comparison posttest, and plots were performed using Prism 9 for macOS version 9.3.1 (GraphPad Software, LLC).

Rotavirus electropherotype. Rotavirus genome extraction and visualization were performed as previously described (96). Briefly, MA104 cells at a density of 3×10^5 cells per well in a 6-well multiwell plate were infected with a virus at MOI of 10 VFU/cell and incubated in 1 mL serum-free DMEM until complete cytopathic effect was reached. The cells and supernatant were harvested, followed by three cycles of liquid nitrogen freeze and 37°C water bath. Then, the samples were mixed vigorously at a ratio of 1:1 with saturated phenol solution pH 4.3 (Merck) and centrifuged for 15 min at 13,000 rpm. The aqueous phase was recovered, and the previous step was repeated. Then, the RNA in the recovered aqueous phase was precipitated by mixing with 0.1 vol 3M Na Acetate at pH 5.2 and 2 vol of 100% ethanol. Samples were incubated for 30 min at -80°C and then centrifuged at 13,000 rpm for 30 min and 4°C. The pellet was resuspended in 15 μL distilled water and mixed with 10 μL Gel Loading dye 6X (New England BioLabs). The samples were migrated in an 8.5% SDS-polyacrylamide gel at 180 volts for 120 min, followed by staining with GelRed Acid gel Stain (Biotium) for 30 min. Images were acquired at Odyssey FC (LI-COR Biosciences).

Transmission electron microscopy. MA104 cells were seeded at 1×10^5 cells in a 2-cm^2 well onto sapphire discs and infected with either rRV/wt or rRV/VP4-BAP at an MOI of 50 VFU/mL. At 6 and 12 hpi, the sapphire discs were collected, fixed with 2.5% glutaraldehyde in 100 mM Na/K-phosphate buffer, pH 7.4, for 1 h at 4°C, and then kept in 100 mM Na/K-phosphate buffer overnight at 4°C. Afterward, samples were postfixed in 1% osmium tetroxide in 100 mM Na/K-phosphate buffer for 1 h at 4°C, dehydrated in a graded ethanol series starting at 70%, followed by two changes in acetone, and embedded in Epon. Ultrathin sections (60 to 80 nm) were cut and stained with uranyl acetate and lead citrate.

For staining biotinylated TLPs with streptavidin-gold, purified particles were dialyzed overnight at 4°C in TNC buffer (10 mM Tris-HCl, pH 7.5, 140 mM NaCl, 10 mM CaCl$_2$). The TLPs were adsorbed for 10 min on carbon-coated Parlodion films mounted on 300-mesh copper grids (EMS). Samples were washed once with water, fixed in 2.5% glutaraldehyde in 100 mM Na/K-phosphate buffer, pH 7.0, for 10 min at room temperature, and washed twice with PBS before incubation for 2 h at room temperature with 10 μL streptavidin conjugated to 10 nm colloidal gold (Sigma-Aldrich, Inc). Before use, the streptavidin-gold conjugate was treated as described previously to separate unconjugated streptavidin from streptavidin-conjugated to colloidal gold (97). The viral particles were washed three times with water and stained with 2% phosphotungstate, pH 7.0, for 1 min at room temperature. Samples were analyzed in a transmission electron microscope (CM12; Philips, Eindhoven, The Netherlands) equipped with coupled device (CCD) cameras (Ultrascan 1000 and Orius SC1000A; Gatan, Pleasanton, CA, USA) at an acceleration voltage of 100 kV.

For calculation of the diameter of virus particles by negative staining, the area of each virus particle was calculated using Imaris software (version 2.1.0/1.53c; Creative Commons license) and then converted to the diameter as follows: $d = 2 \times \sqrt[2]{A/\pi}$, where A is the area and d is the diameter of the particle, respectively.

siRNA reverse transfection. For silencing gs4 of SA11 strain, a siRNA pool of siVP4-25 (5'-uugcucacgaauucuuaauatt-3'), siVP4-931 (5'-gaaguuaccgcacauacuatt-3'), and siVP4-1534 (5'-auug caaugucgcaguuaatt-3') was designed and synthesized by Microsynth AG (Switzerland). siRNA-A (sc-37007, Santa Cruz Biotechnology) was used as negative siRNA control. siRNA reverse transfection was performed by mixing 1.2 μL siRNA 5 μM with 1 μL lipofectamine RNAiMAX transfection reagent (Invitrogen, ThermoFisher Scientific) to a final volume of 100 μL with Opti-MEM (Gibco, ThermoFisher Scientific) per well of a 24-well plate and incubated for 20 min at room temperature. To reach a 10-nM siRNA final concentration, 2×10^4 cells diluted in 500 μL DMEM supplemented with 10% FCS were added on top. Samples were incubated for 60 h prior to analysis. Thus, cells were infected with simian RV strain SA11 at MOI 12 VFU/cell as described previously (25, 92, 93).

FRAP. 1.2×10^4 MA/NSP2 cells per well were seeded in μ-Slide 18-well glass-bottom plates (Ibidi). Cells were RV-infected at MOI of 15 VFU/cell and kept in DMEM-SF. At 4.5 hpi, the cells were counterstained with Hoechst 33342 diluted in FluoroBRITE DMEM (Gibco, Cat. No. A18967-01) at a concentration of 1 μg/mL, incubated for 30 min at 37°C, and subjected to FRAP analysis. FRAP experiments were performed with an SP8 Falcon confocal laser scanning microscope (CLSM) from Leica equipped with a 63$\times$ objective (NA 1.4) using the FRAP function of the LasX software (Leica) as follows: a circular area of 2 μm in diameter, encompassing an entire viroplasm, was bleached with the 405-nm and 481-nm lasers simultaneously, each at 100% laser power, for 20 iterations. The fluorescent recovery was monitored by taking fluorescence images of the mCherry channel every 2 s for 140 s. For each FRAP acquisition, a circular area of 2 μm, encompassing an entire unbleached viroplasm in the same cell, was used as the fluorescent control, and a squared area (5 μm x 5 μm) outside of a cell was chosen as the background. The FRAP data set was analyzed with MatLab (MATLAB R2020b, Mathworks) using the FRAP-tool source code from easyFRAP (Cell Cycle Lab, Medical School, University of Patras). Fully normalized data were used to generate FRAP diagrams and calculate the recovery half-times (T-half) and mobile fractions from independent measurements. Representative images were taken and processed for each FRAP experiment

using the Imaris software v9.5 (Bitplane, Oxford Instruments). Fluorescent intensities of FRAP movies were normalized using a customized Fiji pipeline (95).

Quantitative RT-PCR. MA104 cells at a density of 5×10^5 cells per well in 6-well multiwell plates were RV-infected at an MOI of 18 VFU/cell. The virus was adsorbed for 1 h at 4°C. At 4 hpi, RNA was extracted using a quick RNA miniprepPlus kit (Zymo Research) according to the manufacturer's instructions. cDNA synthesis was prepared with 1 μg of RNA using an AMV reverse transcription system (Promega) and random primers according to the manufacturer's instructions. Then, 2 μL of 1:10 diluted cDNA was mixed with 0.25 μL forward primer (10 pmol/μL), 0.25 μL reverse primer (10 pmol/μL) (Table S2 posted at https://zenodo.org/record/6865927#.YtfEH-xBw-Q), 10 μL SYBR Green PCR master mix (Applied Biosystems), and 7.5 μL nuclease-free water followed by incubation at QuantStudio3 (Applied Biosystems, ThermoFisher Scientific) using standard amplification protocol with an annealing temperature of 60°C. The relative expression of genes was calculated with the formula $2^{-\Delta Ct}$, where ΔCt = Ct target gene − Ct endogenous control gene. HPRT-1, SDHA, and GAPDH were used as endogenous control housekeeping genes. Data were analyzed using Microsoft Excel for MAC (version 16.58). Statistical analysis and plots were done using Prism9 for macOS (version 9.3.1) (GraphPad Software, LLC).

Purification and transfection of DLPs. RV amount sufficient to infect 1×10^6 cells at MOI of 15 VFU/cell was diluted up to 110 μL with TBS. Then, EDTA pH 8.0 was added to a final concentration of 10 mM. The samples were incubated for 1 h at 37°C with gentle mixing and centrifuged at 3,000 rpm for 2 min. The supernatant was recovered, loaded on top of a 100-μL cushion composed of 20% sucrose in PBS, and ultracentrifuged at 20 lb/in^2 for 60 min on an air-driven ultracentrifuge (Airfuge, Beckman Coulter). For quality control, DLPs were monitored by negative staining electron microscopy. The DLPs were normalized using Pierce Coomassie protein assay kit (ThermoFisher Scientific) to determine the amount of total protein followed by an indirect ELISA to normalize to rotavirus protein using as primary antibody a guinea pig antirotavirus, which detected mainly VP6. Thus, DLPs were transfected by diluting them in 12.5 μL Opti-MEM and mixed with 0.75 μL Lipofectamine 2000 (Invitrogen) in 12.5 μL Opti-MEM. The mixture was incubated for 20 min at room temperature and added onto 1×10^4 MA104 cells per well in a 96-well black wall tissue culture plate (Greiner). At 6 hpi, cells were fixed with paraformaldehyde and prepared for immunofluorescence as described above. Images were acquired using a CLSM and then processed with Image J2 version 2.3.0/1.53f.

In-cell western assay. RV-infected MA104 cells (1×10^4) were seeded in a 96-well black tissue culture plate (Greiner). At indicated times postinfection, cells were fixed with 2% paraformaldehyde in PBS for 10 min at room temperature, followed by permeabilization with 0.1% Triton X-100-PBS for 10 min at room temperature. Next, cells were blocked with 2% BSA in PBS for 1 h at room temperature and then incubated with primary antibodies diluted in blocking buffer for 1 h at room temperature in the shaker. Then, the cells were incubated with the corresponding secondary antibody conjugated to IRDye 800 CW (LI-COR). The cell signal was normalized using CellTag 700 stain (LI-COR) diluted at 1:800. The cells were washed three times with 0.01% Tween 20 in PBS between incubations. Samples were acquired using an Odyssey CLx (LI-COR) followed by data analysis and normalization in Microsoft Excel for Mac version 16.58. Statistical analysis, unpaired Student's *t* test, and plots were performed using Prism 9 for macOS version 9.3.1 (GraphPad Software, LLC).

Virus attachment assay. Rotavirus binding was determined by a nonradioactive binding assay as described previously in detail by Zárate et al. (56). The plates were coated with goat antirotavirus (diluted 1:5,000) to capture the virus. In addition, guinea pig antirotavirus (diluted 1:5,000) or streptavidin-HRP (diluted 1:500, Sigma) were used to detect the virus. The reaction was developed using 100 μL of Pierce TMB substrate kit (ThermoFisher) and stopped with 100 μL 1M H_2SO_4. Samples were recorded at an absorbance of 450 nm using an Infinite M Plex (Tecan) plate reader. Data analysis was performed using Microsoft Excel for Mac version 16.58. Statistical analysis, semilog line nonlinear regression, and plots were performed using Prism 9 for macOS version 9.3.1 (GraphPad Software, LLC).

Linear peptide synthesis. The linear peptide was synthesized using an automated peptide synthesis system developed in our laboratory. Here, 200 mg of resin was swelled in 6 mL 100% dimethylformamide (DMF) for 5 min at 60°C with nitrogen bubbling using a Teflon tube of 1/8-inch inner diameter. Importantly, the bubbling with nitrogen is kept during the entire synthesis process. The Fmoc-protecting groups of the resin were removed by washing twice with 6 mL solution of 20% piperidine in DMF. For the first deprotection, the sample was incubated for 1 min at 60°C followed by aspiration. The second deprotection was obtained by incubating for 4 min at 60°C followed by four washes with 7 mL DMF. The coupling of amino acids to unprotected resin or the subsequent unprotected amino acids in the elongated peptide coupled to the resin was performed by twice adding a 7.5-mL mixture of the respective amino acid (5 eq/amine − 3 mL of 200 mM), OxymaPure (7.5 equivalent (eq)/amine − 2 mL of) and DIC (10 eq/amine − 2.5 mL of) dissolved in DMF. The amino acids were coupled twice for 8 min at 60°C with 7 mL DMF wash after the first coupling and three times with 7 mL DMF wash after the second coupling. After each coupling, the newly bound amino acid was deprotected as mentioned above. The coupling reaction time was specifically extended to 10 min for Asp, Glu, and Arg, and temperature was lowered to 50°C for Asp and Glu. The final deprotection was performed in the same manner as explained above. The newly synthesized peptide was washed twice with methanol and dried under vacuum. The peptide cleavage was carried out using TFA/TIS/H2O (94:5:1 vol/vol/vol) for 4 h in 10 mL plastic syringe mounted on a rotter. Then, the peptide was collected in 50 mL tubes, initially with gravity flow and subsequently by inserting the plunger into the syringe. After filtration, the peptide was precipitated with 50 mL ice cold tert-butylmethylether (TBME), centrifuged at 4,400 rpm for 15 min and washed twice with TBME. For purification of the crude peptide, it was dissolved in 10 mL of a solution containing100% mQ-H_2O, 0.1% TFA, subjected to preparative RP-HPLC and obtained

as TFA salt after lyophilization. MS spectra were provided by Mass Spectrometry of the Department of Chemistry and Biochemistry at the University of Bern.

REFERENCES

1. Troeger C, Khalil IA, Rao PC, Cao S, Blacker BF, Ahmed T, Armah G, Bines JE, Brewer TG, Colombara DV, Kang G, Kirkpatrick BD, Kirkwood CD, Mwenda JM, Parashar UD, Petri WA, Riddle MS, Steele AD, Thompson RL, Walson JL, Sanders JW, Mokdad AH, Murray CJL, Hay SI, Reiner RC. 2018. Rotavirus vaccination and the global burden of rotavirus diarrhea among children younger than 5 years. JAMA Pediatr 172:958–965. https://doi.org/10.1001/jamapediatrics.2018.1960.

2. Gomez DE, Weese JS. 2017. Viral enteritis in calves. Can Vet J 58:1267–1274.

3. Vlasova AN, Amimo JO, Saif LJ. 2017. Porcine rotaviruses: epidemiology, immune responses and control strategies. Viruses 9:48. https://doi.org/10.3390/v9030048.

4. Dhama K, Saminathan M, Karthik K, Tiwari R, Shabbir MZ, Kumar N, Malik YS, Singh RK. 2015. Avian rotavirus enteritis—an updated review. Vet Q 35:142–158. https://doi.org/10.1080/01652176.2015.1046014.

5. Lawton JA, Zeng CQ, Mukherjee SK, Cohen J, Estes MK, Prasad BV. 1997. Three-dimensional structural analysis of recombinant rotavirus-like particles with intact and amino-terminal-deleted VP2: implications for the architecture of the VP2 capsid layer. J Virol 71:7353–7360. https://doi.org/10.1128/JVI.71.10.7353-7360.1997.

6. Zhang X, Settembre E, Xu C, Dormitzer PR, Bellamy R, Harrison SC, Grigorieff N. 2008. Near-atomic resolution using electron cryomicroscopy and single-particle reconstruction. Proc Natl Acad Sci U S A 105:1867–1872. https://doi.org/10.1073/pnas.0711623105.

7. Charpilienne A, Lepault J, Rey F, Cohen J. 2002. Identification of rotavirus VP6 residues located at the interface with VP2 that are essential for capsid assembly and transcriptase activity. J Virol 76:7822–7831. https://doi.org/10.1128/jvi.76.15.7822-7831.2002.

8. Lepault J, Petitpas I, Erk I, Navaza J, Bigot D, Dona M, Vachette P, Cohen J, Rey FA. 2001. Structural polymorphism of the major capsid protein of rotavirus. EMBO J 20:1498–1507. https://doi.org/10.1093/emboj/20.7.1498.

9. Li Z, Baker ML, Jiang W, Estes MK, Prasad BV. 2009. Rotavirus architecture at subnanometer resolution. J Virol 83:1754–1766. https://doi.org/10.1128/JVI.01855-08.

10. Settembre EC, Chen JZ, Dormitzer PR, Grigorieff N, Harrison SC. 2011. Atomic model of an infectious rotavirus particle. EMBO J 30:408–416. https://doi.org/10.1038/emboj.2010.322.

11. Yoder JD, Dormitzer PR. 2006. Alternative intermolecular contacts underlie the rotavirus VP5* two- to three-fold rearrangement. EMBO J 25:1559–1568. https://doi.org/10.1038/sj.emboj.7601034.

12. Yoder JD, Trask SD, Vo TP, Binka M, Feng N, Harrison SC, Greenberg HB, Dormitzer PR. 2009. VP5* rearranges when rotavirus uncoats. J Virol 83:11372–11377. https://doi.org/10.1128/JVI.01228-09.

13. Arias CF, Silva-Ayala D, López S, Tsai B. 2015. Rotavirus entry: a deep journey into the cell with several exits. J Virol 89:890–893. https://doi.org/10.1128/JVI.01787-14.

14. Deo RC, Groft CM, Rajashankar KR, Burley SK. 2002. Recognition of the rotavirus mRNA 3′ consensus by an asymmetric NSP3 homodimer. Cell 108:71–81. https://doi.org/10.1016/s0092-8674(01)00632-8.

15. Groft CM, Burley SK. 2002. Recognition of eIF4G by rotavirus NSP3 reveals a basis for mRNA circularization. Mol Cell 9:1273–1283. https://doi.org/10.1016/s1097-2765(02)00555-5.

16. López S, Arias CF. 2012. Rotavirus–host cell interactions: an arms race. Curr Opin Virol 2:389–398. https://doi.org/10.1016/j.coviro.2012.05.001.

17. Montero H, Arias CF, Lopez S. 2006. Rotavirus nonstructural protein NSP3 is not required for viral protein synthesis. J Virol 80:9031–9038. https://doi.org/10.1128/JVI.00437-06.

18. Piron M, Vende P, Cohen J, Poncet D. 1998. Rotavirus RNA-binding protein NSP3 interacts with eIF4GI and evicts the poly (A) binding protein from eIF4F. EMBO J 17:5811–5821. https://doi.org/10.1093/emboj/17.19.5811.

19. Barro M, Patton JT. 2005. Rotavirus nonstructural protein 1 subverts innate immune response by inducing degradation of IFN regulatory factor 3. Proc Natl Acad Sci U S A 102:4114–4119. https://doi.org/10.1073/pnas.0408376102.

20. Patton JT, Silvestri LS, Tortorici MA, Carpio V-D, Taraporewala ZF. 2006. Rotavirus genome replication and morphogenesis: role of the viroplasm. Curr Top Microbiol Immunol 309:169–187.

21. Eichwald C, Rodriguez JF, Burrone OR. 2004. Characterization of rotavirus NSP2/NSP5 interactions and the dynamics of viroplasm formation. J Gen Virol 85:625–634. https://doi.org/10.1099/vir.0.19611-0.

22. Contin R, Arnoldi F, Campagna M, Burrone OR. 2010. Rotavirus NSP5 orchestrates recruitment of viroplasmic proteins. J Gen Virol 91:1782–1793. https://doi.org/10.1099/vir.0.019133-0.

23. Papa G, Borodavka A, Desselberger U. 2021. Viroplasms: assembly and functions of rotavirus replication factories. Viruses 13:1349. https://doi.org/10.3390/v13071349.

24. Fabbretti E, Afrikanova I, Vascotto F, Burrone OR. 1999. Two non-structural rotavirus proteins, NSP2 and NSP5, form viroplasm-like structures *in vivo*. J Gen Virol 80:333–339. https://doi.org/10.1099/0022-1317-80-2-333.

25. Eichwald C, Arnoldi F, Laimbacher AS, Schraner EM, Fraefel C, Wild P, Burrone OR, Ackermann M. 2012. Rotavirus viroplasm fusion and perinuclear localization are dynamic processes requiring stabilized microtubules. PLoS One 7:e47947. https://doi.org/10.1371/journal.pone.0047947.

26. Cheung W, Gill M, Esposito A, Kaminski CF, Courousse N, Chwetzoff S, Trugnan G, Keshavan N, Lever A, Desselberger U. 2010. Rotaviruses associate with cellular lipid droplet components to replicate in viroplasms, and compounds disrupting or blocking lipid droplets inhibit viroplasm formation and viral replication. J Virol 84:6782–6798. https://doi.org/10.1128/JVI.01757-09.

27. Zhou Y, Chen L, Du J, Hu X, Xie Y, Wu J, Lin X, Yin N, Sun M, Li H. 2020. MicroRNA-7 inhibits rotavirus replication by targeting viral NSP5 *in vivo* and *in vitro*. Viruses 12:209. https://doi.org/10.3390/v12020209.

28. Geiger F, Acker J, Papa G, Wang X, Arter WE, Saar KL, Erkamp NA, Qi R, Bravo JPK, Strauss S, Krainer G, Burrone OR, Jungmann R, Knowles TPJ, Engelke H, Borodavka A. 2021. Liquid–liquid phase separation underpins the formation of replication factories in rotaviruses. EMBO J 40:e107711. https://doi.org/10.15252/embj.2021107711.

29. Zambrano JL, Sorondo O, Alcala A, Vizzi E, Diaz Y, Ruiz MC, Michelangeli F, Liprandi F, Ludert JE. 2012. Rotavirus infection of cells in culture induces activation of RhoA and changes in the actin and tubulin cytoskeleton. PLoS One 7:e47612. https://doi.org/10.1371/journal.pone.0047612.

30. Trask SD, McDonald SM, Patton JT. 2012. Structural insights into the coupling of virion assembly and rotavirus replication. Nat Rev Microbiol 10:165–177. https://doi.org/10.1038/nrmicro2673.

31. Arias CF, Romero P, Alvarez V, López S. 1996. Trypsin activation pathway of rotavirus infectivity. J Virol 70:5832–5839. https://doi.org/10.1128/JVI.70.9.5832-5839.1996.

32. Gilbert JM, Greenberg HB. 1998. Cleavage of rhesus rotavirus VP4 after arginine 247 is essential for rotavirus-like particle-induced fusion from without. J Virol 72:5323–5327. https://doi.org/10.1128/JVI.72.6.5323-5327.1998.

33. Dormitzer PR, Nason EB, Prasad BV, Harrison SC. 2004. Structural rearrangements in the membrane penetration protein of a non-enveloped virus. Nature 430:1053–1058. https://doi.org/10.1038/nature02836.

34. Dormitzer PR, Sun ZY, Wagner G, Harrison SC. 2002. The rhesus rotavirus VP4 sialic acid binding domain has a galectin fold with a novel carbohydrate binding site. EMBO J 21:885–897. https://doi.org/10.1093/emboj/21.5.885.

35. Fiore L, Greenberg HB, Mackow ER. 1991. The VP8 fragment of VP4 is the rhesus rotavirus hemagglutinin. Virology 181:553–563. https://doi.org/10.1016/0042-6822(91)90888-i.

36. Graham KL, Halasz P, Tan Y, Hewish MJ, Takada Y, Mackow ER, Robinson MK, Coulson BS. 2003. Integrin-using rotaviruses bind $\alpha2\beta1$ integrin $\alpha2$ I domain via VP4 DGE sequence and recognize $\alpha X\beta2$ and $\alpha V\beta3$ by using VP7 during cell entry. J Virol 77:9969–9978. https://doi.org/10.1128/jvi.77.18.9969-9978.2003.

37. Graham KL, Takada Y, Coulson BS. 2006. Rotavirus spike protein VP5* binds $\alpha2\beta1$ integrin on the cell surface and competes with virus for cell binding and infectivity. J Gen Virol 87:1275–1283. https://doi.org/10.1099/vir.0.81580-0.

38. Estes MK, Graham DY, Gerba CP, Smith EM. 1979. Simian rotavirus SA11 replication in cell cultures. J Virol 31:810–815. https://doi.org/10.1128/JVI.31.3.810-815.1979.

39. Arias CF, López S. 2021. Rotavirus cell entry: not so simple after all. Curr Opin Virol 48:42–48. https://doi.org/10.1016/j.coviro.2021.03.011.

40. Díaz-Salinas MA, Romero P, Espinosa R, Hoshino Y, López S, Arias CF. 2013. The spike protein VP4 defines the endocytic pathway used by rotavirus to enter MA104 cells. J Virol 87:1658–1663. https://doi.org/10.1128/JVI.02086-12.

41. Enouf V, Chwetzoff S, Trugnan G, Cohen J. 2003. Interactions of rotavirus VP4 spike protein with the endosomal protein Rab5 and the prenylated Rab acceptor PRA1. J Virol 77:7041–7047. https://doi.org/10.1128/jvi.77.12.7041-7047.2003.

42. Zárate S, Cuadras MA, Espinosa R, Romero P, Juárez KO, Camacho-Nuez M, Arias CF, López S. 2003. Interaction of rotaviruses with Hsc70 during cell entry is mediated by VP5. J Virol 77:7254–7260. https://doi.org/10.1128/jvi.77.13.7254-7260.2003.

43. Guerrero CA, Bouyssounade D, Zárate S, Isa P, López T, Espinosa R, Romero P, Méndez E, López S, Arias CF. 2002. Heat shock cognate protein 70 is involved in rotavirus cell entry. J Virol 76:4096–4102. https://doi.org/10.1128/jvi.76.8.4096-4102.2002.

44. Li B, Ding S, Feng N, Mooney N, Ooi YS, Ren L, Diep J, Kelly MR, Yasukawa LL, Patton JT, Yamazaki H, Shirao T, Jackson PK, Greenberg HB. 2017. Drebrin restricts rotavirus entry by inhibiting dynamin-mediated endocytosis. Proc Natl Acad Sci U S A 114:E3642–E3651. https://doi.org/10.1073/pnas.1619266114.

45. Condemine W, Eguether T, Couroussé N, Etchebest C, Gardet A, Trugnan G, Chwetzoff S. 2019. The C terminus of rotavirus VP4 protein contains an actin binding domain which requires cooperation with the coiled-coil domain for actin remodeling. J Virol 93:e01598-18. https://doi.org/10.1128/JVI.01598-18.

46. Nejmeddine M, Trugnan G, Sapin C, Kohli E, Svensson L, Lopez S, Cohen J. 2000. Rotavirus spike protein VP4 is present at the plasma membrane and is associated with microtubules in infected cells. J Virol 74:3313–3320. https://doi.org/10.1128/jvi.74.7.3313-3320.2000.

47. Trejo-Cerro Ó, Eichwald C, Schraner EM, Silva-Ayala D, López S, Arias CF. 2018. Actin-dependent nonlytic rotavirus exit and infectious virus morphogenetic pathway in nonpolarized cells. J Virol 92:e02076-17. https://doi.org/10.1128/JVI.02076-17.

48. Gardet A, Breton M, Fontanges P, Trugnan G, Chwetzoff S. 2006. Rotavirus spike protein VP4 binds to and remodels actin bundles of the epithelial brush border into actin bodies. J Virol 80:3947–3956. https://doi.org/10.1128/JVI.80.8.3947-3956.2006.

49. Gardet A, Breton M, Trugnan G, Chwetzoff S. 2007. Role for actin in the polarized release of rotavirus. J Virol 81:4892–4894. https://doi.org/10.1128/JVI.02698-06.

50. Wolf M, Vo PT, Greenberg HB. 2011. Rhesus rotavirus entry into a polarized epithelium is endocytosis dependent and involves sequential VP4 conformational changes. J Virol 85:2492–2503. https://doi.org/10.1128/JVI.02082-10.

51. Predonzani A, Arnoldi F, López-Requena A, Burrone OR. 2008. In vivo site-specific biotinylation of proteins within the secretory pathway using a single vector system. BMC Biotechnol 8:41. https://doi.org/10.1186/1472-6750-8-41.

52. De Lorenzo G, Eichwald C, Schraner EM, Nicolin V, Bortul R, Mano M, Burrone OR, Arnoldi F. 2012. Production of in vivo-biotinylated rotavirus particles. J Gen Virol 93:1474–1482. https://doi.org/10.1099/vir.0.040089-0.

53. Laimbacher AS, Esteban LE, Castello AA, Abdusetir Cerfoglio JC, Argüelles MH, Glikmann G, D'Antuono A, Mattion N, Berois M, Arbiza J, Hilbe M, Schraner EM, Seyffert M, Dresch C, Epstein AL, Ackermann M, Fraefel C. 2012. HSV-1 amplicon vectors launch the production of heterologous rotavirus-like particles and induce rotavirus-specific immune responses in mice. Mol Ther 20:1810–1820. https://doi.org/10.1038/mt.2012.108.

54. Kanai Y, Kobayashi T. 2021. Rotavirus reverse genetics systems: development and application. Virus Res 295:198296. https://doi.org/10.1016/j.virusres.2021.198296.

55. Jiménez-Zaragoza M, Yubero MP, Martín-Forero E, Castón JR, Reguera D, Luque D, de Pablo PJ, Rodríguez JM. 2018. Biophysical properties of single rotavirus particles account for the functions of protein shells in a multilayered virus. Elife 7:e37295. https://doi.org/10.7554/eLife.37295.

56. Zárate S, Espinosa R, Romero P, Méndez E, Arias CF, López S. 2000. The VP5 domain of VP4 can mediate attachment of rotaviruses to cells. J Virol 74:593–599. https://doi.org/10.1128/jvi.74.2.593-599.2000.

57. Dormitzer PR, Greenberg HB, Harrison SC. 2000. Purified recombinant rotavirus VP7 forms soluble, calcium-dependent trimers. Virology 277:420–428. https://doi.org/10.1006/viro.2000.0625.

58. Shaw RD, Vo PT, Offit PA, Coulson BS, Greenberg HB. 1986. Antigenic mapping of the surface proteins of rhesus rotavirus. Virology 155:434–451. https://doi.org/10.1016/0042-6822(86)90205-9.

59. Papa G, Venditti L, Arnoldi F, Schraner EM, Potgieter C, Borodavka A, Eichwald C, Burrone OR. 2019. Recombinant rotaviruses rescued by reverse genetics reveal the role of NSP5 hyperphosphorylation in the assembly of viral factories. J Virol 94:e01110-19. https://doi.org/10.1128/JVI.01110-19.

60. Déctor MA, Romero P, López S, Arias CF. 2002. Rotavirus gene silencing by small interfering RNAs. EMBO Rep 3:1175–1180. https://doi.org/10.1093/embo-reports/kvf234.

61. Martínez JL, Eichwald C, Schraner EM, López S, Arias CF. 2022. Lipid metabolism is involved in the association of rotavirus viroplasms with endoplasmic reticulum membranes. Virology 569:29–36. https://doi.org/10.1016/j.virol.2022.02.005.

62. Shutova MS, Svitkina TM. 2018. Mammalian nonmuscle myosin II comes in three flavors. Biochem Biophys Res Commun 506:394–402. https://doi.org/10.1016/j.bbrc.2018.03.103.

63. Limouze J, Straight AF, Mitchison T, Sellers JR. 2004. Specificity of blebbistatin, an inhibitor of myosin II. J Muscle Res Cell Motil 25:337–341. https://doi.org/10.1007/s10974-004-6060-7.

64. Trask SD, Dormitzer PR. 2006. Assembly of highly infectious rotavirus particles recoated with recombinant outer capsid proteins. J Virol 80:11293–11304. https://doi.org/10.1128/JVI.01346-06.

65. Herrmann T, Torres R, Salgado EN, Berciu C, Stoddard D, Nicastro D, Jenni S, Harrison SC. 2021. Functional refolding of the penetration protein on a non-enveloped virus. Nature 590:666–670. https://doi.org/10.1038/s41586-020-03124-4.

66. Abdelhakim AH, Salgado EN, Fu X, Pasham M, Nicastro D, Kirchhausen T, Harrison SC. 2014. Structural correlates of rotavirus cell entry. PLoS Pathog 10:e1004355. https://doi.org/10.1371/journal.ppat.1004355.

67. Salgado EN, Garcia Rodriguez B, Narayanaswamy N, Krishnan Y, Harrison SC. 2018. Visualization of calcium ion loss from rotavirus during cell entry. J Virol 92:e01327-18. https://doi.org/10.1128/JVI.01327-18.

68. Salgado EN, Upadhyayula S, Harrison SC. 2017. Single-particle detection of transcription following rotavirus entry. J Virol 91:e00651-17. https://doi.org/10.1128/JVI.00651-17.

69. Trask SD, Kim IS, Harrison SC, Dormitzer PR. 2010. A rotavirus spike protein conformational intermediate binds lipid bilayers. J Virol 84:1764–1770. https://doi.org/10.1128/JVI.01682-09.

70. Bunnell TM, Burbach BJ, Shimizu Y, Ervasti JM. 2011. β-Actin specifically controls cell growth, migration, and the G-actin pool. Mol Biol Cell 22:4047–4058. https://doi.org/10.1091/mbc.E11-06-0582.

71. Trejo-Cerro O, Aguilar-Hernández N, Silva-Ayala D, López S, Arias CF. 2019. The actin cytoskeleton is important for rotavirus internalization and RNA genome replication. Virus Res 263:27–33. https://doi.org/10.1016/j.virusres.2019.01.003.

72. Beckett D, Kovaleva E, Schatz PJ. 1999. A minimal peptide substrate in biotin holoenzyme synthetase-catalyzed biotinylation. Protein Sci 8:921–929. https://doi.org/10.1110/ps.8.4.921.

73. Fairhead M, Howarth M. 2015. Site-specific biotinylation of purified proteins using BirA. Methods Mol Biol 1266:171–184. https://doi.org/10.1007/978-1-4939-2272-7_12.

74. Roux KJ, Kim DI, Burke B. 2013. BioID: a screen for protein-protein interactions. Curr Protoc Protein Sci 74:19.23.1–19.23.14.

75. Vesikari T, Clark HF, Offit PA, Dallas MJ, DiStefano DJ, Goveia MG, Ward RL, Schödel F, Karvonen A, Drummond JE, DiNubile MJ, Heaton PM. 2006. Effects of the potency and composition of the multivalent human-bovine (WC3) reassortant rotavirus vaccine on efficacy, safety and immunogenicity in healthy infants. Vaccine 24:4821–4829. https://doi.org/10.1016/j.vaccine.2006.03.025.

76. Ruiz-Palacios GM, Pérez-Schael I, Velázquez FR, Abate H, Breuer T, Clemens SC, Cheuvart B, Espinoza F, Gillard P, Innis BL, Cervantes Y, Linhares AC, López P, Macías-Parra M, Ortega-Barría E, Richardson V, Rivera-Medina DM,

Rivera L, Salinas B, Pavía-Ruz N, Salmerón J, Rüttimann R, Tinoco JC, Rubio P, Nuñez E, Guerrero ML, Yarzábal JP, Damaso S, Tornieporth N, Sáez-Llorens X, Vergara RF, Vesikari T, Bouckenooghe A, Clemens R, De Vos B, O'Ryan M, Group HRVS. 2006. Safety and efficacy of an attenuated vaccine against severe rotavirus gastroenteritis. N Engl J Med 354:11–22. https://doi.org/10.1056/NEJMoa052434.

77. Ito N, Takayama-Ito M, Yamada K, Hosokawa J, Sugiyama M, Minamoto N. 2003. Improved recovery of rabies virus from cloned cDNA using a vaccinia virus-free reverse genetics system. Microbiol Immunol 47:613–617. https://doi.org/10.1111/j.1348-0421.2003.tb03424.x.

78. Guglielmi KM, McDonald SM, Patton JT. 2010. Mechanism of intraparticle synthesis of the rotavirus double-stranded RNA genome. J Biol Chem 285:18123–18128. https://doi.org/10.1074/jbc.R110.117671.

79. Arnold M, Patton JT, McDonald SM. 2009. Culturing, storage, and quantification of rotaviruses. Curr Protoc Microbiol 15:15C.3.1–15C.3.24. https://doi.org/10.1002/9780471729259.mc15c03s15.

80. Fuerst TR, Niles EG, Studier FW, Moss B. 1986. Eukaryotic transient-expression system based on recombinant vaccinia virus that synthesizes bacteriophage T7 RNA polymerase. Proc Natl Acad Sci U S A 83:8122–8126. https://doi.org/10.1073/pnas.83.21.8122.

81. Yusa K, Zhou L, Li MA, Bradley A, Craig NL. 2011. A hyperactive piggyBac transposase for mammalian applications. Proc Natl Acad Sci U S A 108:1531–1536. https://doi.org/10.1073/pnas.1008322108.

82. Papa G, Venditti L, Braga L, Schneider E, Giacca M, Petris G, Burrone OR. 2020. CRISPR-Csy4-mediated editing of rotavirus double-stranded RNA genome. Cell Rep 32:108205. https://doi.org/10.1016/j.celrep.2020.108205.

83. Kanai Y, Komoto S, Kawagishi T, Nouda R, Nagasawa N, Onishi M, Matsuura Y, Taniguchi K, Kobayashi T. 2017. Entirely plasmid-based reverse genetics system for rotaviruses. Proc Natl Acad Sci U S A 114:2349–2354. https://doi.org/10.1073/pnas.1618424114.

84. Komoto S, Kanai Y, Fukuda S, Kugita M, Kawagishi T, Ito N, Sugiyama M, Matsuura Y, Kobayashi T, Taniguchi K. 2017. Reverse genetics system demonstrates that rotavirus nonstructural protein NSP6 is not essential for viral replication in cell culture. J Virol 91:e00695-17. https://doi.org/10.1128/JVI.00695-17.

85. Eichwald C, Vascotto F, Fabbretti E, Burrone OR. 2002. Rotavirus NSP5: mapping phosphorylation sites and kinase activation and viroplasm localization domains. J Virol 76:3461–3470. https://doi.org/10.1128/jvi.76.7.3461-3470.2002.

86. Sun M, Giambiagi S, Burrone O. 1997. VP4 protein of simian rotavirus strain SA11 expressed by a baculovirus recombinant. Zhongguo Yi Xue Ke Xue Yuan Xue Bao 19:48–53. (In Chinese.)

87. Petris G, Bestagno M, Arnoldi F, Burrone OR. 2014. New tags for recombinant protein detection and O-glycosylation reporters. PLoS One 9:e96700. https://doi.org/10.1371/journal.pone.0096700.

88. Bellinzoni RC, Mattion NM, Burrone O, Gonzalez A, La Torre JL, Scodeller EA. 1987. Isolation of group A swine rotaviruses displaying atypical electropherotypes. J Clin Microbiol 25:952–954. https://doi.org/10.1128/jcm.25.5.952-954.1987.

89. Arnoldi F, Campagna M, Eichwald C, Desselberger U, Burrone OR. 2007. Interaction of rotavirus polymerase VP1 with nonstructural protein NSP5 is stronger than that with NSP2. J Virol 81:2128–2137. https://doi.org/10.1128/JVI.01494-06.

90. Cesaratto F, Sasset L, Myers MP, Re A, Petris G, Burrone OR. 2019. BiP/GRP78 mediates ERAD targeting of proteins produced by membrane-bound ribosomes stalled at the STOP-codon. J Mol Biol 431:123–141. https://doi.org/10.1016/j.jmb.2018.10.009.

91. Campagna M, Eichwald C, Vascotto F, Burrone OR. 2005. RNA interference of rotavirus segment 11 mRNA reveals the essential role of NSP5 in the virus replicative cycle. J Gen Virol 86:1481–1487. https://doi.org/10.1099/vir.0.80598-0.

92. Buttafuoco A, Michaelsen K, Tobler K, Ackermann M, Fraefel C, Eichwald C. 2020. Conserved rotavirus NSP5 and VP2 domains interact and affect Viroplasm. J Virol 94:e01965-19. https://doi.org/10.1128/JVI.01965-19.

93. Eichwald C, De Lorenzo G, Schraner EM, Papa G, Bollati M, Swuec P, de Rosa M, Milani M, Mastrangelo E, Ackermann M, Burrone OR, Arnoldi F. 2018. Identification of a small molecule that compromises the structural integrity of viroplasms and rotavirus double-layered particles. J Virol 92:e01943-17. https://doi.org/10.1128/JVI.01943-17.

94. Glück S, Buttafuoco A, Meier AF, Arnoldi F, Vogt B, Schraner EM, Ackermann M, Eichwald C. 2017. Rotavirus replication is correlated with S/G2 interphase arrest of the host cell cycle. PLoS One 12:e0179607. https://doi.org/10.1371/journal.pone.0179607.

95. Schindelin J, Arganda-Carreras I, Frise E, Kaynig V, Longair M, Pietzsch T, Preibisch S, Rueden C, Saalfeld S, Schmid B, Tinevez JY, White DJ, Hartenstein V, Eliceiri K, Tomancak P, Cardona A. 2012. Fiji: an open-source platform for biological-image analysis. Nat Methods 9:676–682. https://doi.org/10.1038/nmeth.2019.

96. Chen D, Gombold JL, Ramig RF. 1990. Intracellular RNA synthesis directed by temperature-sensitive mutants of simian rotavirus SA11. Virology 178:143–151. https://doi.org/10.1016/0042-6822(90)90387-7.

97. Bauer M, Smith GP. 1988. Filamentous phage morphogenetic signal sequence and orientation of DNA in the virion and gene-V protein complex. Virology 167:166–175. https://doi.org/10.1016/0042-6822(88)90066-9.